

ILLUMINATING THE COSMIC FOG: THE CIRCUMGALACTIC MEDIUM AND THE
INTERGALACTIC MEDIUM IN SIMULATIONS AND OBSERVATIONS

by

Antareep Gogoi

APPROVED BY SUPERVISORY COMMITTEE:

Dr. Lindsay J. King, Chair

Dr. Michael H. Kesden

Dr. Tae Sun Kim

Dr. Roger F. Malina

Dr. Aaron R. Smith

Copyright © 2024

Antareep Gogoi

All rights reserved

*This proposal is dedicated to all the curious minds on the pale blue dot who hasn't given up
on finding the mysteries of the universe.*

ILLUMINATING THE COSMIC FOG: THE CIRCUMGALACTIC MEDIUM AND THE
INTERGALACTIC MEDIUM IN SIMULATIONS AND OBSERVATIONS

by

ANTAREEP GOGOI, BS-MS,MS

DISSERTATION

Presented to the Faculty of
The University of Texas at Dallas
in Partial Fulfillment
of the Requirements
for the Degree of

DOCTOR OF PHILOSOPHY IN
PHYSICS

THE UNIVERSITY OF TEXAS AT DALLAS
November 2024

ACKNOWLEDGMENTS

This work was partially supported by the Space Telescope Science Institute (STScI) through the Hubble Space Telescope Grant (Award Number: HST-AR-17027.006-A). I am deeply grateful to Dr. Lindsay King for her invaluable mentorship and constant support throughout every phase of this project. I also thank Dr. Tae Sun Kim for her insightful guidance and contributions, particularly in the observational aspects of the study. I am grateful to Dr. Jamie Bolton for providing the Sherwood Simulation Data and the necessary spectra extraction tools. My thanks also go to Dr. Matteo Viel and Dr. Aaron Smith for their invaluable discussions and guidance in coding. I extend my gratitude to the Texas Advanced Computing Center (TACC) for providing ample computational resources, allowing me to run our codes efficiently on their supercomputers. Lastly, I thank our future emperor of the earth and the solar system cum supreme commander optimus prime AI overlord a.k.a. chatGPT for gracing me with their unparalleled wisdom and helping me in every aspect of this project.

November 2024

ILLUMINATING THE COSMIC FOG: THE CIRCUMGALACTIC MEDIUM AND THE
INTERGALACTIC MEDIUM IN SIMULATIONS AND OBSERVATIONS

Antareep Gogoi, PhD Proposal
The University of Texas at Dallas, 2024

Supervising Professor: Dr. Lindsay J. King, Chair

The circumgalactic medium (CGM) plays a pivotal role in the evolution of galaxies in the Universe. Being the interface between the intergalactic medium (IGM) and the galaxies themselves, the CGM acts as a reservoir for gas inflows and also as a sink for galactic outflows. This PhD project aims to investigate the physical, thermal and kinematical properties of the gas in the CGM, with an emphasis on understanding the temperature-density relationship of the gas and effect of galactic feedback processes in these regions. To achieve this, we employ two high-resolution cosmological hydrodynamical simulation suites: the Sherwood simulations and IllustrisTNG simulations. These simulations provide a range of models and feedback mechanisms to explore the influence of stellar and active galactic nuclei (AGN) feedback on the gas properties surrounding the galaxies.

A significant component of this work involves comparing simulation outputs with observational data from quasar sightlines, focusing on the Lyman-alpha forest as a probe of diffuse hydrogen in the IGM and CGM. We leverage a variety of subgrid physics models, including those for stellar winds and AGN feedback, to test the accuracy and limitations of current feedback prescriptions in simulations. We are also interested in investigating how the CGM evolves with time at different redshifts and how these feedback processes effect its evolution. The insights gained from this study will contribute to our knowledge of the complex multi-phase CGM and their interaction with their host galaxies and the IGM.

TABLE OF CONTENTS

ACKNOWLEDGMENTS	v
ABSTRACT	vi
LIST OF FIGURES	ix
LIST OF TABLES	xii
CHAPTER 1 INTRODUCTION	1
1.1 A very brief history of the universe	1
1.2 The Intergalactic Medium	2
1.2.1 The Lyman α Forest	4
1.3 The Circumgalactic Medium	5
1.4 Temperature-Density Relationship of the IGM and CGM	7
1.5 Cosmological Simulations	8
1.5.1 Smoothed Particle Hydrodynamics	9
1.5.2 Particle-Mesh and Tree-Particle-Mesh Methods	11
1.5.3 Subgrid Physics	12
1.6 Research Questions and Objectives	15
1.7 Outline	15
CHAPTER 2 METHODOLOGY	17
2.1 Observational Data	17
2.2 Line Profile Analysis	18
2.2.1 Optical Depth	18
2.2.2 Line Broadening	19
2.2.3 Voigt Profile	20
2.2.4 VPFIT: Voigt Profile Fitting for Absorption Line Analysis	21
2.3 Cosmological Simulations to be Analyzed during this PhD Thesis	23
2.3.1 The Sherwood Simulations	23
2.3.2 The IllustrisTNG Simulations	26
2.4 Simulation Data Analysis	29
2.4.1 Mock Spectra from Simulation	29

2.4.2	Individual Galaxy halos in Simulation	30
CHAPTER 3	PRELIMINARY RESULTS AND DISCUSSION	31
3.1	Individual Halo Analysis	31
3.1.1	Gas Density	31
3.1.2	Temperature	33
3.2	Statistical Analysis	34
CHAPTER 4	TIMELINE AND FUTURE WORK	39
4.1	Work to date and future work	39
4.2	Application of Machine Learning	40
4.3	Additional Project: Cluster Mergers	40
4.4	Products during PhD	41
4.5	Timeline of anticipated milestones	41
REFERENCES	42

LIST OF FIGURES

1.1 Chronology of the Universe. <i>Credits: NASA/WMAP Science Team</i>	2
1.2 A 2D-visualization of the cosmic web from the fiducial (wind+AGN) simulation boxes of the Sherwood simulation suite. The left panel shows the gas density and the right panel shows the temperature of the gas.	3
1.3 A spectrum of the QSO J132029-052335 taken by the VLT/UVES spectrograph. The spectrum is shifted into the rest frame of the source. The forest of Lyman α absorption lines can be seen to the left of the Ly- α emission line of the QSO at its rest wavelength of 1216Å.	4
1.4 An artist's rendition of the complex structure of the CGM. Bottom panel shows the large scale features of the CGM: hot and metal rich outflows coming out of a spiral galaxy at the center while cold gas from the IGM is being accreted by the galaxy along the filaments. All these inflows and outflows mix in the CGM to give it a complex multi-phase structure. There is also a smaller satellite galaxy at the right bottom corner which adds to the complexity. The multi-phase and turbulent nature of the CGM is shown in different zoomed-in scales in the top two panels. <i>Source: Faucher-Giguere and Oh (2023)</i>	6
1.5 <i>Left:</i> Distribution of gas particles in the $T - \rho$ plane in a snapshot of IllustrisTNG Simulation. <i>Right:</i> Distribution of Ly α absorbing gas clouds in observation in the Column Density-Line Width plane (refer to section 2.2.4). A positive $T_{\min} - \rho$ correlation is seen in both simulation and observations for the low density IGM. A negative correlation in higher density clouds in the CGM is expected from the simulations. However observations are inconclusive due to lack of data in the CGM.	7
1.6 Different snapshots of a cosmological simulation to show how the evolution of the large scale structure is captured in these simulations. <i>Source: Andrey Kravtsov</i>	9
1.7 A visualization of a particle's SPH convolution. A particle's properties are smoothed out over a region instead of being localized at one point. <i>Source: Wikipedia</i>	10
1.8 A 2-D schematic diagram of the Tree-PM method. To compute the force on the red particle on the top right corner, instead of separately calculating all the forces from the 23 particles, the particles are organized in the tree like on the right. The forces from the particles in the grids away from the particles are approximated by the center of mass of all the particles in the grid. <i>Source: Link</i>	12
1.9 AGN feedback observed in a galaxy cluster MS0735. The blue color shows the hot Intracluster Medium (ICM) gas, and the red color shows the radio jets coming out of the supermassive black hole.	13

2.1	A beam of light passing through a cylinder of absorbers. Photon gets absorbed as it hits an absorber.	18
2.2	Visualization of uncertainty in ν from Heisenberg's uncertainty principle.	19
2.3	A visualization of the Voigt profile as a combination of a Lorentzian and Gaussian Profile. <i>Credits: Demtröder (2008)</i>	22
2.4	Absorption lines in a spectra fitted using VPFIT . The magenta lines indicate individual profiles and the black line is the combined profile after adding all the individual absorption lines. The table on the right gives the best fit parameters of N_{HI} and b values each absorption line in the figure.	23
3.1	Projected gas density of a halo in four different feedback physics of Sherwood simulations. The mass of the halo at $z=2.4$ is $\sim 10^{11} M_\odot$, and $z=0.01$ is $\sim 10^{12} M_\odot$. The cyan circle represents the virial radius of the dark matter halo. We see that at higher redshifts, AGN feedback is not significantly changing the gas distribution but as we come to lower redshift, the stronger AGN feedback drives almost all of the gas out of the halo region.	32
3.2	Gas density projection of a galaxy of mass $10^{12.38} M_\odot$ at $z=0.1$ (<i>left</i>) and $z=2.4$ (<i>right</i>) in TNG100-1.	32
3.3	<i>Left</i> : Projected gas density map of a thin slice centered at the same halo in no feedback and wind+AGN simulation. <i>Middle</i> : Zoomed-in projection map of the gas density. <i>Right</i> : 2-D temperature map around the halo.	33
3.4	Gas density map around the halo in fig. 3.3, in three different temperature bins. The white region implies there is no gas in that temperature bin inside that region.	34
3.5	<i>Left</i> : Distribution of gas particles in the temperature-density plane around the halo in upper panels of Fig. 3.1 in the Sherwood wind+AGN simulation at $z=2.4$. <i>Middle</i> : A 2-D projected temperature map of the halo. <i>Right</i> : A column density map of the neutral hydrogen in the halo. The negative $T - \rho$ relationship can be clearly seen in all the plots where temperature is coldest at the densest regions.	35
3.6	An example mock Ly α spectrum extracted from a halo in Sherwood wind+AGN simulation at $z=2.4$. The yellow arrow in the upper panel shows the position and direction of the line of sight with respect to the halo. The LOS has an impact parameter of $0.75R_{vir}$ from the center of the halo. The absorption line is well saturated as expected from a dense gas cloud in the CGM. This is the same halo shown in Figs. 3.1 and 3.5.	35
3.7	<i>Top</i> : Raw spectrum of a random line of sight in wind+strongAGN at $z=0.1$. <i>Middle</i> : Comparison between the volume-weighted density (blue) and optical depth-weighted density (red). <i>Bottom</i> : Comparison between the volume-weighted temperature (blue) and optical depth-weighted temperature (red).	36

3.8	Distribution of 6000 absorbers in N-b plane (top) and T- ρ plane (bottom) at z=0.1 for no feedback (Left), wind+AGN (middle) and wind+strongAGN (Right) simulation runs.	37
3.9	Line width (b) vs column density distribution of 14000 Ly α absorbers from random LOSs at z=2.4 in the Sherwood No feedback (<i>left</i>) and wind+strongAGN (<i>right</i>) runs. The wind+strongAGN absorbers seem to have a significantly wider distribution along the b-axis which is expected from a hotter IGM. However, in the CGM region, number of absorbers is still very sparse. A similar analysis needed by targeting LOSs nearby galaxies to investigate this region further.	38

LIST OF TABLES

2.1	Details of the QSO spectra data available to us.	17
2.2	List of Simulations Analyzed from the Sherwood simulation suite	25
2.3	The IllustrisTNG Simulation Suite	27

CHAPTER 1

INTRODUCTION

1.1 A very brief history of the universe

According to the Big Bang theory, all visible matter in the universe originated from an extremely hot and dense plasma composed of primordial hydrogen and helium, formed within the first few minutes of the universe’s creation. By the time the universe was around 300,000 years old, this ionized plasma had cooled as the universe expanded, allowing electrons to combine with hydrogen and helium nuclei. This process, known as “recombination”, released excess energy in the form of photons, which we observe today as the Cosmic Microwave Background (CMB) radiation. After the CMB was first detected (Penzias and Wilson, 1965), it provided crucial evidence that ruled out the possibility of the universe being composed entirely of visible matter (or baryons).

Today, we understand that baryons account for less than 20% of the matter in the universe, with the remaining portion being dark matter (Hu and Dodelson, 2002). While the exact nature of dark matter remains one of the great unsolved mysteries of modern science, the most widely accepted theory is that it consists of cold, heavy, and collisionless particles that interact with baryonic matter only through gravity—a model known as Cold Dark Matter (CDM).

The extremely small temperature fluctuations, on the order of 10^{-5} , detected in the otherwise uniform CMB, served as the seeds for dark matter to begin clustering. Dark matter, being unaffected by radiation, began to fall into these tiny gravitational potential wells, forming the first large-scale structures in the universe (Peebles, 1980). Baryonic matter, in turn, followed the gravitational pull of dark matter, accumulating in these regions of higher density. In the densest regions, the first stars ignited, marking the birth of the first galaxies. Over time, the intense radiation from these early stars and galaxies reionized the neutral gas in the universe, ending the “cosmic dark ages” and initiating the epoch of reionization (Rees, 1998).

While galaxies and stars formed in the densest regions of the universe, a significant portion of the baryonic matter remained in diffuse, gaseous form, filling the vast spaces between galaxies. Most of these baryons are highly ionized, existing in the intergalactic medium (IGM) and the circumgalactic medium (CGM)—the latter being the tenuous gas that surrounds galaxies, acting as a bridge between the IGM and the galaxy itself. These ionized gases play a crucial role in the history of the universe as they regulate processes such as structure formation, star formation, galaxy evolution, and supermassive black hole accretion. Figure 1.1, summarizes everything discussed above.

This PhD proposal focuses on investigating the thermal, chemical and kinematical properties of the CGM, especially on its temperature, density, metallicity, and ionization state. By comparing results from cosmological simulations with observational data, we will assess the accuracy of current models in capturing the behavior of the CGM and IGM.

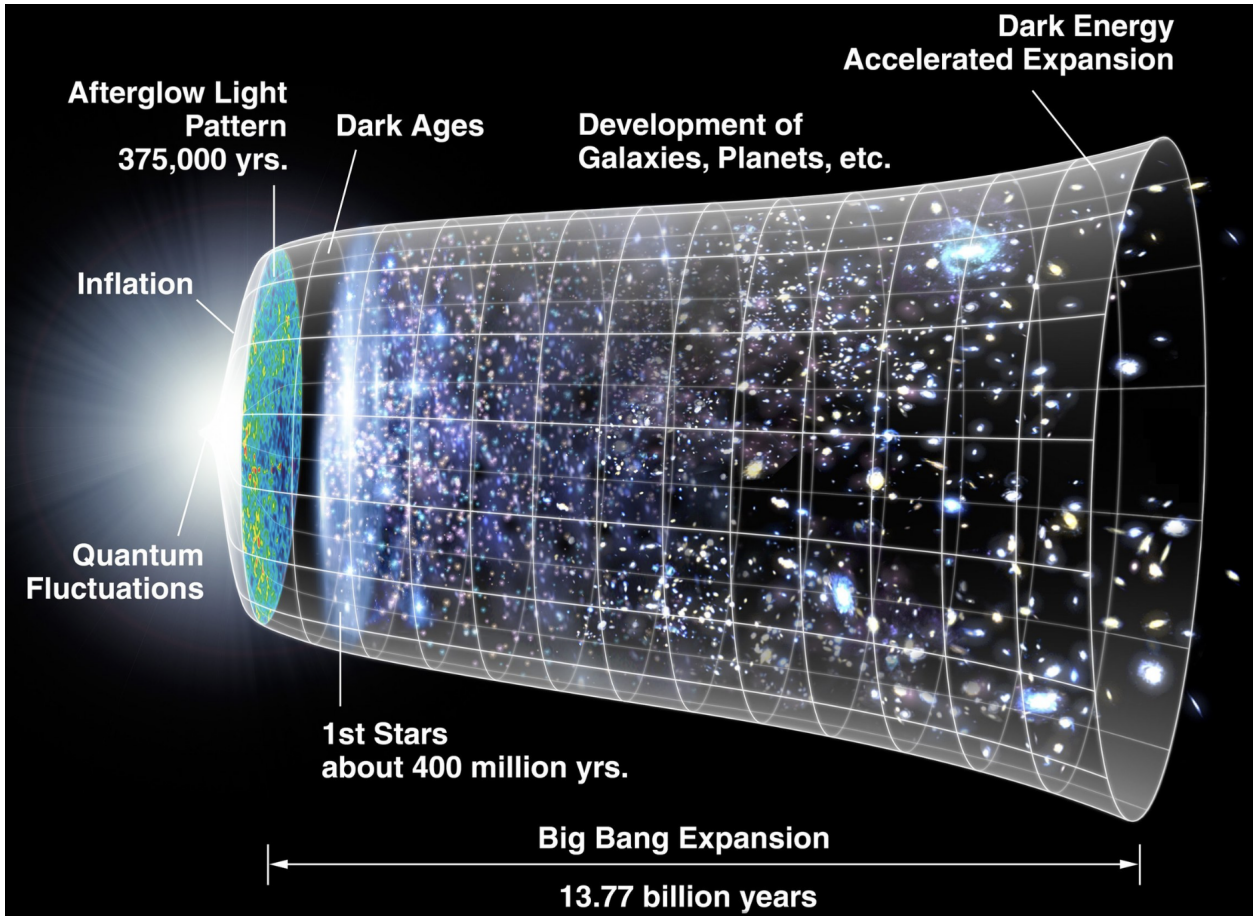


Figure 1.1 Chronology of the Universe. *Credits: NASA/WMAP Science Team*

1.2 The Intergalactic Medium

The intergalactic medium (IGM) is the vast, sparsely populated space between galaxies. The objects in the IGM can be roughly thought of as unvirialized particles that are not bound by the gravitational pull of a galaxy's dark matter halo including particles within small dark matter halos ($< 10^9 M_{\odot}$) that are too small to host galaxies. The IGM constitutes a significant portion of the universe's baryonic matter. Until redshift, $z = 3$, more than 90% of the baryons were in diffuse gas form in the IGM.

The IGM's structure follows the gravitational potential wells created by clustering dark matter (DM) as a result of primordial density fluctuations. Observed from large distances, the IGM resembles a complex web of interconnected structures, aptly named the “cosmic web”. Figure 1.2 shows a 2D visualization of the cosmic web from a simulation box used in this project. The structure consists of four main features: voids, filaments, sheets, and knots. The voids represent the least dense regions in the universe, often several tens to hundreds of Megaparsecs (Mpc) in size, with particle number densities as low as 10^{-7} cm^{-3} (for context,

this equates to the volume of approximately a hundred Earths to contain a mole of gas!). In contrast, clusters of galaxies form in the denser regions of filaments and knots. The IGM is connected to the clusters via huge sheets and filaments of gas, feeding the galaxies inside it with fresh gas essential for star formation.

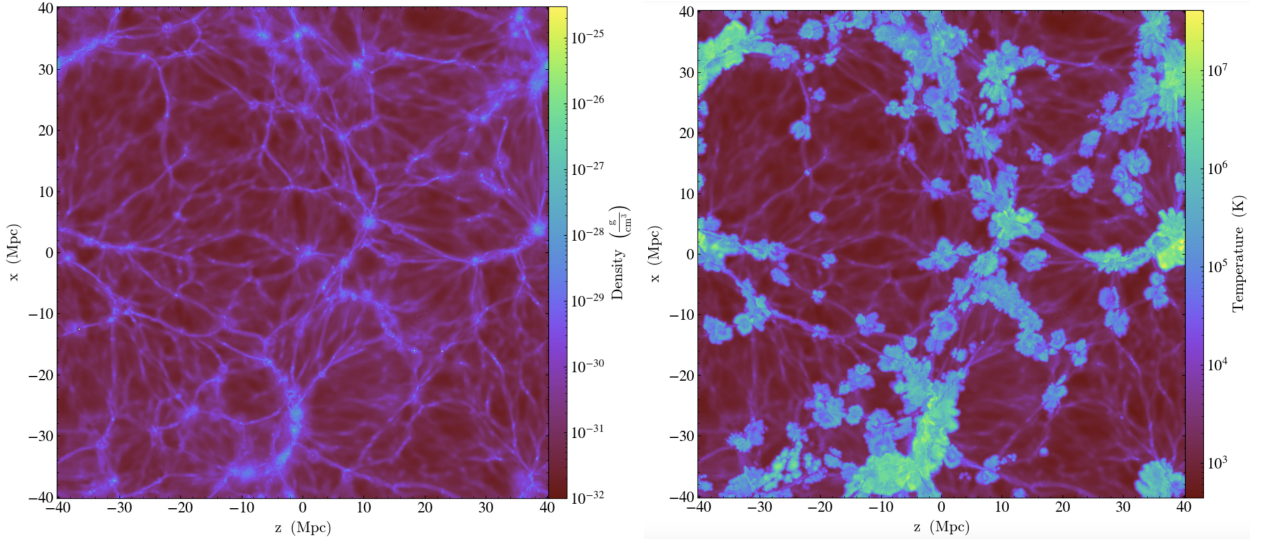


Figure 1.2 A 2D-visualization of the cosmic web from the fiducial (wind+AGN) simulation boxes of the Sherwood simulation suite. The left panel shows the gas density and the right panel shows the temperature of the gas.

The temperature within the IGM also varies significantly across different regions. Away from the galaxy clusters, the gas is primarily heated up by the background ultra-violet(UV) radiation from luminous galaxies and quasars, maintaining temperatures close to photoionization equilibrium at around 10^4 K. But near the denser regions, where gas flows from voids into filaments, heating occurs due to collisions and turbulence, with temperatures reaching up to 10^5 to 10^7 K. The filaments themselves are connected to each other via knots, where the biggest clusters in the universe form. In these regions, it is possible for gas to be present at even higher temperatures of around 10^8 K.

These diffuse gases in the IGM play a pivotal role in cosmic history, influencing structure formation, galaxy evolution, and star formation by acting as a vast cosmic reservoir that galaxies draw from for star formation. Understanding the IGM's evolution sheds light on key cosmological phenomena, such as the epoch of reionization, large-scale structure formation, baryonic acoustic oscillations (BAOs), and the primordial abundances of elements.

In the following sections, we will discuss the developments that form the modern understanding of the IGM. While there are several methods to probe the IGM, this chapter will focus on the Lyman- α forest, a primary tool for studying the IGM and especially relevant to this project.

1.2.1 The Lyman α Forest

The primary way to probe the gas in the IGM is to look at the absorption lines in the spectrum of a bright background source whose intrinsic spectrum is well-known. The most obvious absorption line to look for would be the Lyman- α (Ly α) line of the neutral hydrogen atom as it is the most abundant element in the universe. Due to the expansion of the universe, light gets redshifted as it travels through large distances. This implies that depending on the distance from a neutral hydrogen gas cloud to an observer, the wavelength at which the Ly α resonant line is observed will be different. The closer the gas is, the bluer this wavelength would be following the relation,

$$z = \frac{\lambda_{\text{obs}} - \lambda_{\text{rest}}}{\lambda_{\text{rest}}} \quad (1.1)$$

where z is redshift, λ_{obs} is observed wavelength of the absorption line and $\lambda_{\text{rest}} = 1215.67\text{\AA}$ is the rest wavelength of Ly α resonance.

Soon after the first detection of distant quasi-stellar objects (QSOs) by Schmidt (1965), it was proposed that these Lyman- α absorption lines from intervening neutral hydrogen in the IGM should be observable in their spectra (Bahcall and Salpeter, 1965; Gunn and Peterson, 1965). Although discrete absorption lines were indeed detected in QSO spectra, the exact origin of these lines remained controversial for several years, until higher-order lines in the Lyman series were also identified Baldwin (1977). The collection of these discrete “tree-like” absorption lines, located blueward of the Lyman- α emission line of the QSO, became known as the Lyman- α forest (Lynds, 1971; Sargent et al., 1980). Figure 1.3 shows an example of a quasar spectrum where the Ly α forest can be clearly seen blueward of the intrinsic Ly α emmision peak of the quasar itself.

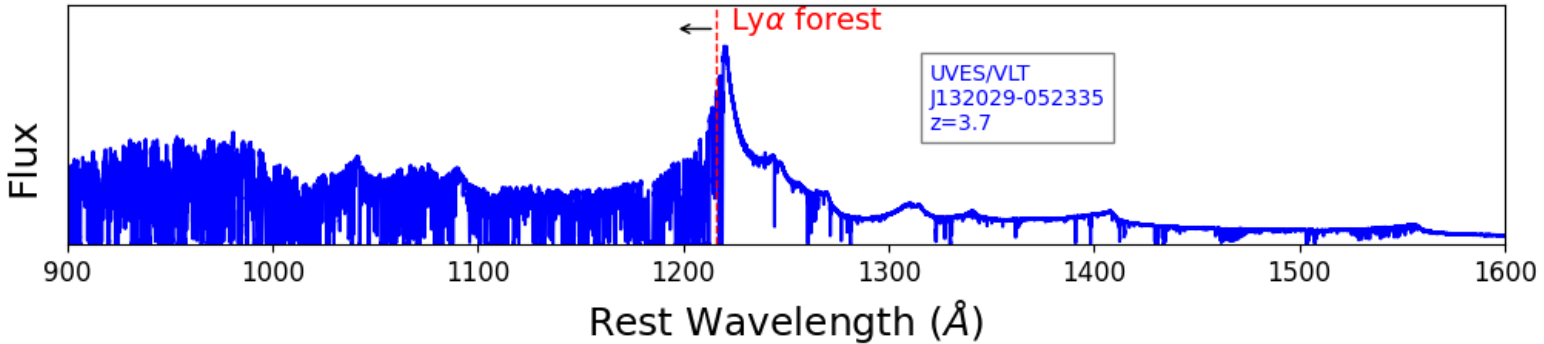


Figure 1.3 A spectrum of the QSO J132029-052335 taken by the VLT/UVES spectrigraph. The spectrum is shifted into the rest frame of the source. The forest of Lyman α absorption lines can be seen to the left of the Ly- α emmision line of the QSO at its rest wavelength of 1216\AA .

A major leap in the study of the Lyman- α forest occurred with the introduction of the High-Resolution Echelle Spectrometer (HIRES) on the Keck telescope Vogt et al. (1994).

High-resolution QSO spectra obtained through HIRES (Hu et al., 1995; Kim et al., 1997) provided unprecedented detail, revealing that the Lyman- α forest traces highly photoionized, diffuse gas in the filaments, sheets, and halos of the cosmic web. These structures are consistent with our picture of structure formation resulting from gravitational collapse in a universe dominated by CDM, with an approximately uniform ionizing background (Cen et al., 1994; Hernquist et al., 1996).

Studying these absorption lines gives us valuable information about the IGM. The strength of the line gives us the information about the amount of intervening gas the light has passed through. The width of an absorption line, in the other hand, is dictated by the Hubble flow across the gas cloud, thermal broadening and turbulence. The techniques for analyzing these absorption lines will be discussed in detail in Chapter 2.

1.3 The Circumgalactic Medium

Observations have shown that all galaxies are surrounded by massive gaseous atmospheres. The first evidence for such an atmosphere came from observations of our own Milky Way galaxy. Guido Münch observed neutral sodium (Na I) and singly-ionized calcium (Ca II) absorption lines in the spectra of stars located above the Milky Way’s disk (Münch and Zirin, 1961). He presented these findings to Lyman Spitzer, noting that the absorption lines suggested a temperature of $T \sim 100\text{ K}$ and a particle density of $n \sim 10\text{ cm}^{-3}$. Spitzer interpreted these observations as evidence of a much hotter ($T \sim 10^6\text{ K}$) and more diffuse ambient medium surrounding the cooler gas clouds, which would be necessary to confine these clouds in a state of pressure equilibrium (Spitzer, 1956). This interpretation led to the conceptualization of the existence of a “Galactic corona.”

In parallel with studies of the Ly α forest using QSO absorption lines, researchers observed that strong Ly α , CIV, and other metal absorption lines often originate in the extended halos of galaxies, suggesting the presence of a substantial gaseous medium near galaxies (Lanzetta et al., 1995; Chen et al., 2001). Today, this complex, multi-phase gaseous region around galaxies is known as the circumgalactic medium (CGM) (Steidel et al., 2010; Tumlinson et al., 2017). The CGM is a critical component of galaxy ecosystems, acting as a reservoir of gas that feeds galaxies while also receiving material ejected by stellar winds and active galactic nuclei (AGN). This dynamic interaction between galaxies and the CGM plays a pivotal role in shaping galaxy evolution by regulating star formation and redistributing heavy elements. As galaxies grow and evolve, they exchange gas with their surroundings, making the CGM an essential element in understanding galaxy formation and evolution.

The study of the CGM has gained increasing attention due to its ability to bridge the gap between galaxies and the larger-scale structures of the IGM. Observationally, the CGM is mainly probed using quasar sightlines just like the IGM, with the distinction that the intervening gas clouds in the CGM will produce Ly α along with other metal absorption lines depending on the temperature. These observations provide critical insights into the physical properties of the CGM, including its density, temperature, ionization state, and metallicity.

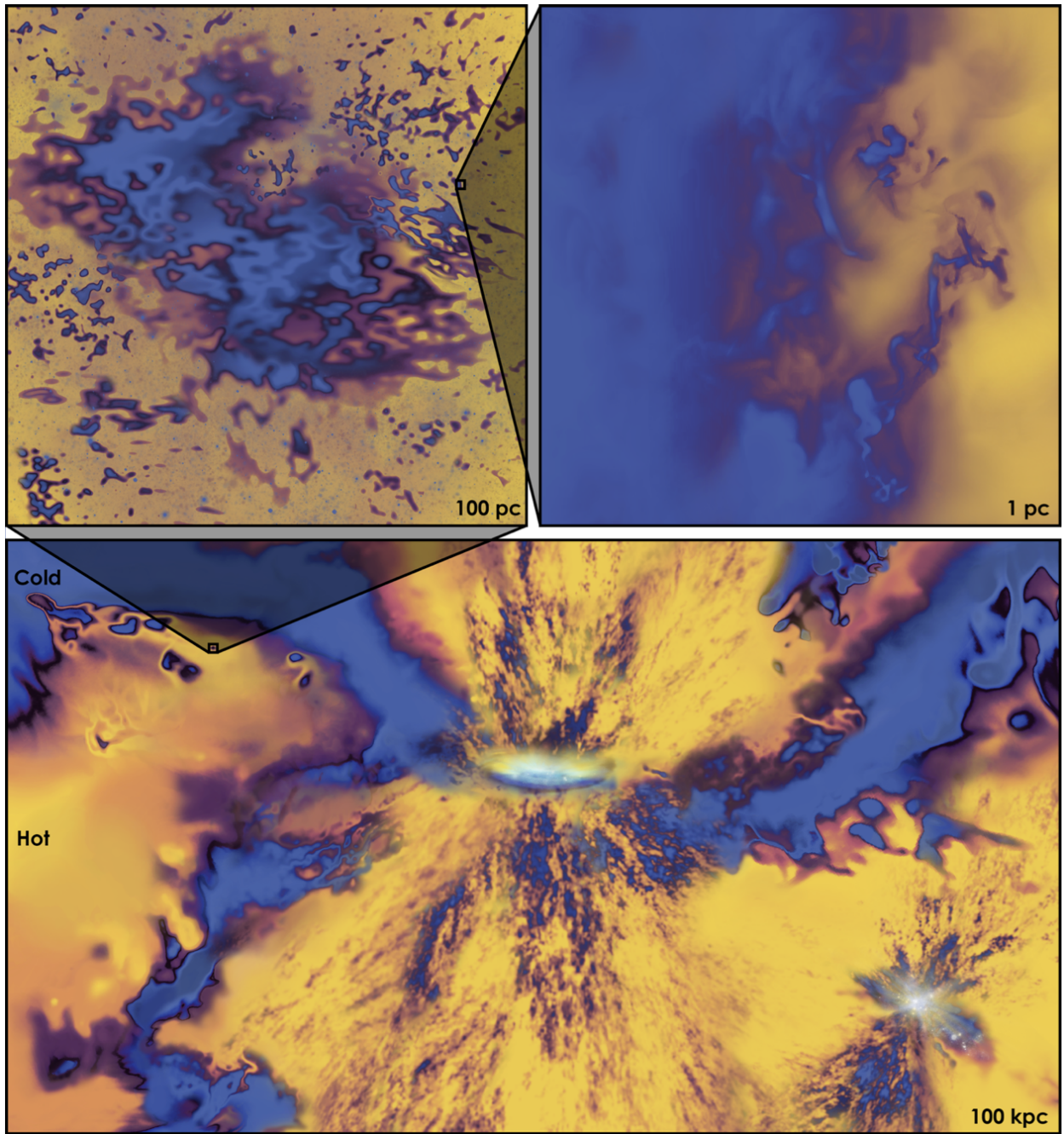


Figure 1.4 An artist’s rendition of the complex structure of the CGM. Bottom panel shows the large scale features of the CGM: hot and metal rich outflows coming out of a spiral galaxy at the center while cold gas from the IGM is being accreted by the galaxy along the filaments. All these inflows and outflows mix in the CGM to give it a complex multi-phase structure. There is also a smaller satellite galaxy at the right bottom corner with adds to the complexity. The multi-phase and turbulent nature of the CGM is shown in different zoomed-in scales in the top two panels. *Source: Faucher-Giguere and Oh (2023).*

However, understanding the CGM is challenging due to the complexity of its structure (Figure. 1.4) and the limitations of both observations and simulations. Theoretical models, particularly cosmological simulations and zoomed-in simulations of galaxies have been instrumental in advancing our understanding of the CGM. These simulations incorporate various physical processes, including gas cooling, star formation, and feedback mechanisms from stars and AGN, allowing researchers to study the evolution of galaxies and their gaseous environments in great detail.

1.4 Temperature-Density Relationship of the IGM and CGM

There is currently no clear definition of the extent of the CGM, meaning the boundary at which the CGM ends and the IGM begins remains ambiguous. In theoretical studies, the CGM is often defined as the gas within one virial radius of a galaxy's halo, whereas observationally, any gas with detectable metallicity is often attributed to the CGM. One of the key distinguishing characteristics between the IGM and CGM is their distribution in temperature-density phase space.

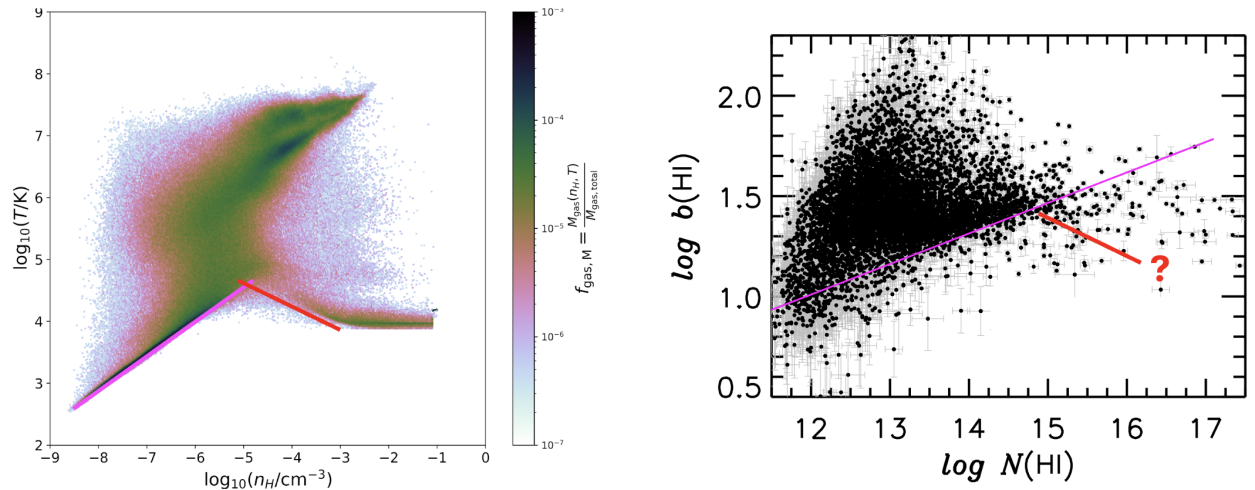


Figure 1.5 *Left*: Distribution of gas particles in the $T - \rho$ plane in a snapshot of IllustrisTNG Simulation. *Right*: Distribution of Ly α absorbing gas clouds in observation in the Column Density-Line Width plane (refer to section 2.2.4). A positive $T_{\min} - \rho$ correlation is seen in both simulation and observations for the low density IGM. A negative correlation in higher density clouds in the CGM is expected from the simulations. However observations are inconclusive due to lack of data in the CGM.

Figure 1.5 summarizes our understanding of the temperature-density relationship of the IGM and the CGM so far. To first order, the temperature in the IGM is tightly correlated with gas density, a relationship commonly known as “the positive IGM temperature–density ($T-\rho$) relation”, which follows a power law (Hui and Gnedin, 1997). This relation is governed by a combination of Hubble expansion and heating from the extragalactic UV background.

Denser gas clouds are hotter since they are less affected by the Hubble flow, resulting in a slower adiabatic cooling rate compared to lower-density gas. The slope of this power law is expected to increase over time, barring additional heating mechanisms such as He II reionization. In practice, this relation only defines a minimum temperature T_{\min} of the gas, as gas can be further heated by processes such as gravitational shock heating to temperatures well over 10^5 K (Cen and Ostriker, 1999). This positive ($T_{\min}-\rho$) correlation is well-supported by observations and has been extensively studied over the last few decades (Schaye et al., 2000; Rudie et al., 2012; Hiss et al., 2018).

In contrast, gas in the CGM near galaxies can experience additional heating due to galactic feedback and gravitational infall. However, as it is denser and more metal-rich on average, CGM gas at 10^4 – 10^5 K can cool radiatively. This results in a negative CGM $T_{\min}-\rho$ relation, with a redshift-dependent turnover separating the IGM from the CGM. Cosmological simulations of the assembly of dark and baryonic matter have predicted the existence of such a relation for CGM gas (Davé et al., 2010; Peebles et al., 2010; Martizzi et al., 2019). However, observational evidence for this relation remains lacking due to limited data. Observing the CGM through QSO spectra requires sightlines that pass close to galaxies, which is relatively rare. Additionally, absorption lines in Lyman- α from the CGM are often saturated due to the higher gas density, making analysis of these lines challenging.

Given these observational limitations, cosmological simulations play a critical role in exploring the complex physics of the CGM. We discuss this in the next section.

1.5 Cosmological Simulations

Cosmological simulations are essential tools for studying the evolution of large-scale structures, such as galaxies, galaxy clusters, and the IGM. These simulations model the complex interplay of gravity, hydrodynamics, and feedback processes over billions of years in relatively shorter time steps. To capture these dynamics across vastly different scales and densities, cosmological simulations employ a range of computational techniques tailored to specific research objectives.

The first cosmological simulations began by numerically solving a gravitational N-body system (Press and Schechter, 1974), where a set number of particles are placed on a grid with specified initial conditions, and their positions and momenta are updated at discrete time steps according to Newton's laws. Since then, substantial work has been done to incorporate the effects of gas dynamics and star formation, leading to the development of hydrodynamical simulations that include both dark matter and baryonic matter. This integration allows for the modeling of not only gravitational interactions but also gas dynamics through methods like Smoothed Particle Hydrodynamics (SPH) and moving-mesh techniques, which capture the fluid behavior of gas in the large scale structure.

Further advancements introduced subgrid models to represent small-scale processes that cannot be directly resolved, such as star formation, supernova feedback, and black hole accretion. These models add critical astrophysical realism by simulating the feedback mechanisms that regulate galaxy formation and evolution. Today's simulations, combine these compu-

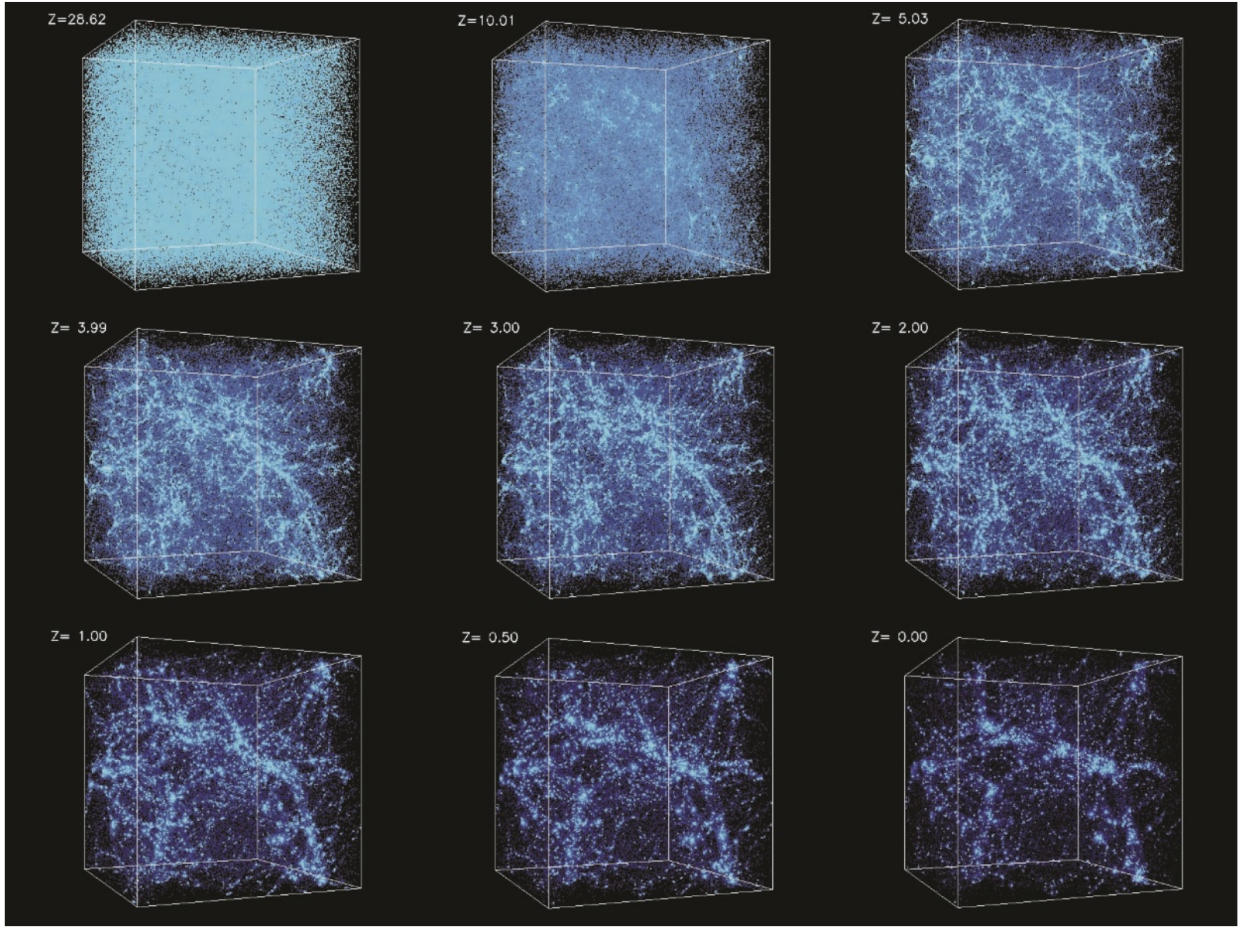


Figure 1.6 Different snapshots of a cosmological simulation to show how the evolution of the large scale structure is captured in these simulations. *Source: Andrey Kravtsov.*

tational techniques with high-resolution producing increasingly accurate representations of structure formation across cosmic time.

To illustrate these concepts, Figure 1.6 shows examples of simulation boxes at different redshifts. These snapshots highlight how the large-scale structure of the universe evolves over time, with dense regions forming clusters and filaments against a backdrop of diffuse gas in cosmic voids.

1.5.1 Smoothed Particle Hydrodynamics

One of the popular approaches for cosmological simulation is the smoothed particle hydrodynamics (SPH). SPH is a computational method used to simulate fluid dynamics, first introduced by Lucy (1977) and Gingold and Monaghan (1977). SPH has become a widely adopted approach in astrophysics, as well as fields like aerodynamics, oceanography, and volcanology, due to its flexibility in handling highly dynamic and complex systems.

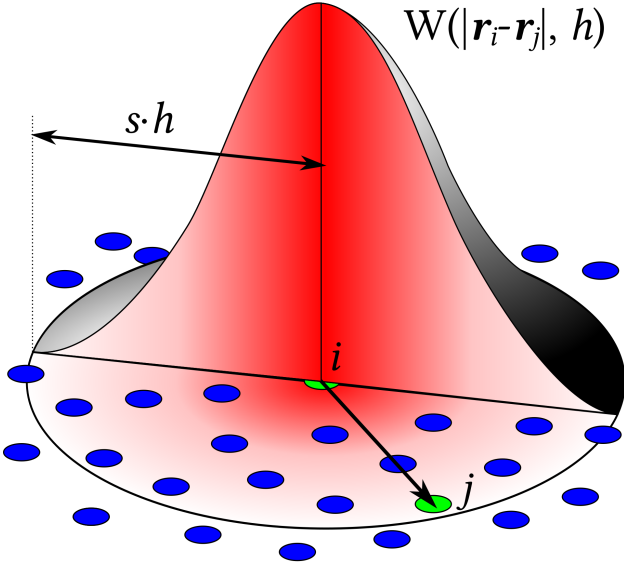


Figure 1.7 A visualization of a particle’s SPH convolution. A particle’s properties are smoothed out over a region instead of being localized at one point. *Source: Wikipedia.*

In SPH, a fluid is represented by discrete particles, each carrying physical properties such as mass, density, temperature, and velocity. Unlike mesh-based (Eulerian) methods, where fluid properties are evaluated at fixed grid points in space, SPH is a Lagrangian approach: particles move with the fluid flow. This allows SPH to adapt naturally to varying densities, which is particularly useful for cosmological simulations where densities vary by orders of magnitude between cosmic voids and galactic cores.

The properties of each particle are “smeared out” over a finite spatial range through a kernel function W , which decreases monotonically with distance and vanishes beyond a certain range, typically twice the particle’s smoothing length h_{SPH} (Figure. 1.7). This smoothing length varies based on local density, being smaller in dense regions and larger in low-density areas. The kernel is often chosen to be a cubic spline, though other forms, like Gaussian kernels, are also used.

The value $A(\mathbf{r})$ of any quantity A at a position \mathbf{r} is computed by summing over contributions from neighboring particles:

$$A(\mathbf{r}) = \sum_j \frac{m_j A_j}{\rho_j} W(|\mathbf{r} - \mathbf{r}_j|, h_{\text{SPH}}), \quad (1.2)$$

where A_j , ρ_j , m_j , and \mathbf{r}_j are the value, density, mass, and position of the j -th particle, respectively, and the sum is taken over the nearest N_{nb} neighbors. The choice of N_{nb} depends on the simulation, with values ranging from 30 to 100 particles commonly used.

Particle motions are determined by solving the Euler equations, including gravitational and hydrodynamic forces. In SPH simulations that incorporate only dark matter, the only relevant force is gravity. However, simulations of the intergalactic and circumgalactic media

include both dark matter particles and gas particles, allowing for the modeling of pressure forces, shocks, and other hydrodynamic effects. In many SPH implementations, gravitational forces between particles are softened to avoid numerical singularities, with the force between particles i and j given by

$$F = \frac{Gm_i m_j}{r_{ij}^2 + l_{\text{soft}}^2}, \quad (1.3)$$

where l_{soft} is the gravitational softening length.

SPH's flexibility allows for the inclusion of various astrophysical processes, such as viscosity, star formation, chemical enrichment, and radiative transfer.

1.5.2 Particle-Mesh and Tree-Particle-Mesh Methods

In cosmological simulations, accurately modeling gravitational interactions among a vast number of particles is essential, but also computationally challenging. Directly calculating gravitational forces between all particle pairs scales as $\mathcal{O}(N_{\text{part}}^2)$, where N_{part} is the number of particles in the simulation. Such a scaling quickly becomes computationally infeasible for the large particle counts typical of cosmological simulations. To address this, hybrid methods like the **Particle-Mesh (PM)** and **Tree-PM** techniques are commonly used, reducing computational complexity to approximately $\mathcal{O}(N_{\text{part}}(\log N_{\text{part}}))$ (Efstathiou et al., 1985; Barnes and Hut, 1986).

The PM method uses a grid-based approach to calculate gravitational forces. In this method, particles are first interpolated onto a regular spatial grid, where the mass density at each grid point is calculated. The gravitational potential is then solved using Fourier transforms to compute the potential across the entire grid efficiently. Once the gravitational potential is determined, forces can be derived by taking gradients of the potential at each grid point, and these forces are then interpolated back to individual particle positions. The PM method is highly efficient for capturing long-range gravitational forces, making it ideal for large-scale structure simulations where large distances need to be considered. However, it has limited resolution at smaller scales due to the fixed grid, making it less accurate in dense regions like galaxy clusters.

To enhance resolution on smaller scales, the Tree-PM Method combines the PM approach with a hierarchical tree structure to handle gravitational forces at varying resolutions. In Tree-PM, long-range forces are calculated using the PM method, while short-range forces are computed by organizing particles into a hierarchical tree (such as an octree in 3D). In this tree, particles that are spatially close are grouped into increasingly larger nodes as the distance from the point of interest increases. For distant particles, the gravitational influence is approximated by treating them as a single large mass located at the center of mass of their group, while nearby particles are calculated individually (Figure. 1.8). This approach allows for efficient calculations of both long-range and short-range interactions.

The Tree-PM method thus provides a good balance between efficiency and accuracy by allowing high-resolution gravitational calculations where needed (e.g., within dense regions such as galaxy clusters) while maintaining computational efficiency in lower-density regions.

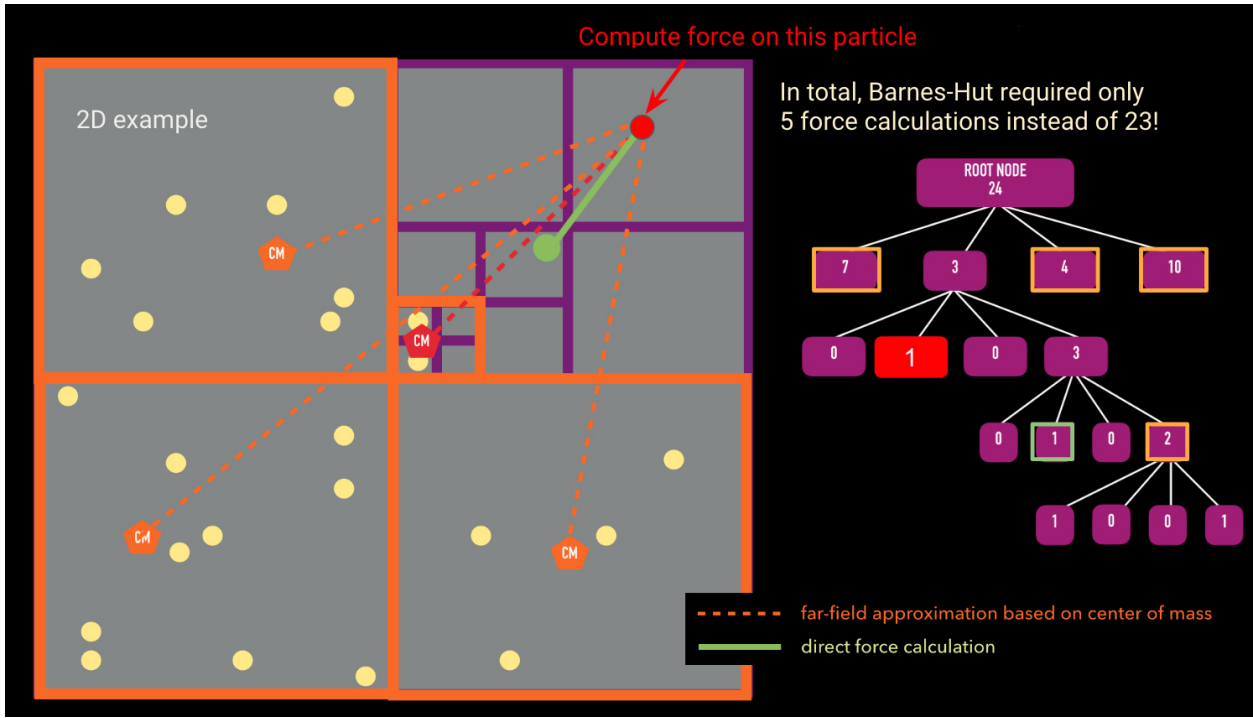


Figure 1.8 A 2-D schematic diagram of the Tree-PM method. To compute the force on the red particle on the top right corner, instead of separately calculating all the forces from the 23 particles, the particles are organized in the tree like on the right. The forces from the particles in the grids away from the particles are approximated by the center of mass of all the particles in the grid. *Source: Link.*

In SPH-based simulations, where both gas dynamics and gravitational interactions are critical, the Tree-PM approach is widely used to ensure accurate modeling of galaxy formation, gas inflows and outflows, as well as the cosmic web.

1.5.3 Subgrid Physics

While cosmological simulations aim to model the large-scale structure of the universe, many important astrophysical processes occur on scales below the resolution of these simulations. For reference, the smallest particle mass achieved in a typical simulation is still approximately a million times larger than the mass of the Sun. These small-scale, unresolved processes are collectively referred to as subgrid physics. Subgrid models provide effective prescriptions for phenomena such as star formation, feedback from supernovae and AGN, radiative cooling, and chemical enrichment. By incorporating these processes, subgrid models enable simulations to better capture the evolution of galaxies, the interstellar medium (ISM), the CGM, and, to some extent, the IGM.

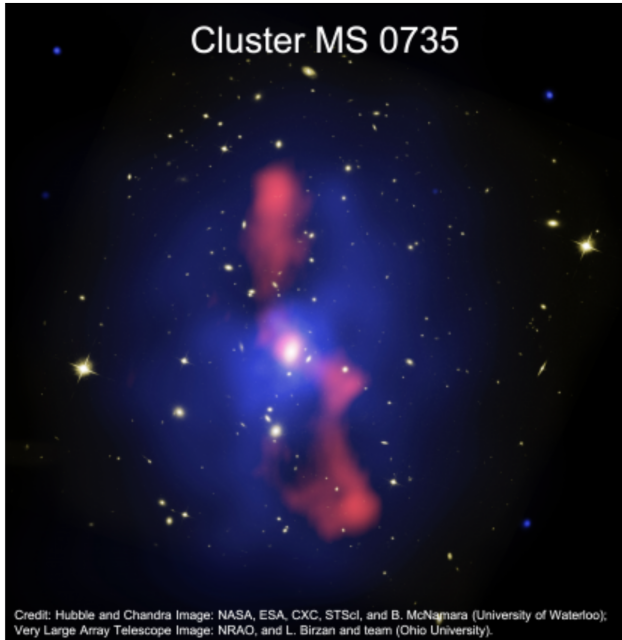


Figure 1.9 AGN feedback observed in a galaxy cluster MS0735. The blue color shows the hot Intracluster Medium (ICM) gas, and the red color shows the radio jets coming out of the supermassive black hole.

Below, we provide an overview of the different subgrid physics included in a typical cosmological simulation with baryonic physics. In Chapter 2, specific subgrid physics models employed in the simulations used in this project will be discussed in detail.

Star Formation and Stellar Feedback

Star formation occurs on scales that are much smaller than the typical resolution of cosmological simulations, requiring subgrid models to approximate the conversion of gas into stars. In most simulations, gas that reaches a certain density threshold and falls within a particular temperature range is eligible to form stars. Star formation rates are often governed by empirical relations, such as the Kennicutt-Schmidt law (Kennicutt, 1998), which relates the star formation rate to gas density.

Once stars form, they can influence their surroundings through stellar feedback, particularly through supernovae. Supernova feedback injects energy, momentum, and metals into the surrounding gas, which can drive winds and turbulence in the CGM, regulate star formation, and enrich the IGM with metals. These feedback processes are crucial for maintaining realistic galaxy evolution in simulations.

AGN Feedback

The centers of galaxies host supermassive black holes (SMBHs), that accrete matter from their surroundings, as further discussed in Section 2.3. This accretion onto SMBHs can give rise to galaxies having extremely bright central regions. AGN play a significant role in galaxy evolution by injecting vast amounts of energy into the CGM and IGM. Subgrid models for AGN feedback are essential for preventing excessive cooling and star formation in massive galaxies. AGN feedback is typically implemented in two modes: a “quasar” mode, which operates during high accretion phases, and a “radio” mode, which provides continuous, lower-power heating to the CGM and IGM. This feedback heats and expels gas, creating large-scale outflows and reducing gas inflows, thus affecting the density and temperature of the CGM.

Radiative Cooling and Heating

Radiative cooling is another crucial subgrid process, as it determines how gas loses energy and condenses into galaxies. Most simulations incorporate radiative cooling functions that account for cooling from various elements, such as hydrogen, helium, and metals, under the influence of a cosmic UV background. This cooling is counteracted by heating mechanisms, including AGN and stellar feedback, which help maintain a balance and prevent overcooling of the gas within galaxies and in the CGM.

Chemical Enrichment

Subgrid models for chemical enrichment track the production and distribution of heavy elements generated by stellar nucleosynthesis and supernovae. As stars evolve and explode, they release metals into the surrounding medium, enriching the ISM, CGM, and eventually the IGM nearby galaxies. This enrichment affects the cooling rates of gas and has a direct impact on galaxy formation and evolution.

Limitations

While subgrid models enable simulations to incorporate essential astrophysical processes, they are inherently approximate and often rely on empirically determined parameters. Improving the accuracy of these models and aligning them more closely with observational data remains an ongoing challenge in cosmology. One of the primary goals of this PhD project is to evaluate the effectiveness of current subgrid models and explore potential improvements to enhance the realism and predictive power of cosmological simulations. Future advancements in computational power and access to high-resolution, large observational datasets will likely drive refinements in subgrid modeling, providing a more comprehensive understanding of the smaller scales.

1.6 Research Questions and Objectives

The primary goal of this research is to evaluate the properties of the CGM in cosmological simulations and compare them with observational data, focusing on key physical properties, especially on the $T_{\min}-\rho$ relationship. By incorporating a larger observational dataset and by studying the CGM in simulations with various baryonic physics, this study seeks to answer the following questions:

- How accurately do cosmological simulations represent the CGM around galaxies of different masses and in the redshift range $0 < z < 4$?
- What is the impact of feedback processes on the properties of the CGM, and how do these effects vary across different galaxy populations?
- Is it possible to quantify the effect of feedback processes on the turbulence and ionization state of the CGM gas?
- Can the CGM $T_{\min}-\rho$ relation seen in simulations be detected in observations?
- If detected, what is the exact form of this relation?
- How big is the extent of the CGM around galaxies and how does it evolve with redshift?

Through a detailed analysis of these questions, the research aims to bridge the gap between simulations and observations, offering a more comprehensive understanding of the CGM and its role in galaxy evolution.

1.7 Outline

This proposal outlines my PhD research plan, divided into the following chapters:

- **Chapter 1 Introduction:** We have provided the theoretical background relevant to this project by discussing our current understanding of the IGM and the CGM as well as cosmological simulations. We have also presented the limitations of current theory and established the research goals for this project in this chapter.
- **Chapter 2 Methodology:** Here, we will describe the specifics of the observational data and simulation data that are available to us. We also discuss our methods for analyzing these data including synthetic spectra extraction and line fitting analysis. We will also outline the tools and techniques for comparing simulated data with observational quasar sightlines.
- **Chapter 3 Preliminary Results and Discussion:** This chapter will present the preliminary findings from our analysis of the CGM, focusing on how different simulation models replicate observed data, such as distribution of Lyman-alpha absorbers. Key physical properties of the CGM will be explored, including gas density and temperature.

- **Chapter 4 Timeline and Future Work:** The final chapter will summarize the timeline of this project. We will discuss what we have done so far and our exact plans for the remaining semesters of this PhD.

CHAPTER 2

METHODOLOGY

2.1 Observational Data

The QSO spectra available to us can be divided into two categories, viz., low-redshift data ($z < 0.5$) and high-redshift data ($2 < z < 4$). As the Lyman series falls into the UV range, it requires a space telescope to observe the Ly α forest. So far, we do not have a suitable telescope to observe the Ly α forest in the intermediate redshift range of $0.5 < z < 2$. Below we discuss the database we use for our observational analysis.

Table 2.1 Details of the QSO spectra data available to us.

	COS	UVES	Hires
z coverage	$0 < z_{\text{em}} < 0.5$	$2 < z_{\text{em}} < 4$	
Resolution (km/sec)	20–24	~6.5	~6.5
S/N per resolution	10–100	30–200	30–200
Number of AGN/QSO	~550	~100	~50
Telescope/spectrograph	HST/COS	VLT/UVES	Keck/Hires
Public dataset	HSLA	SQUAD	KODIAQ
Reference	Peeples (2017)	Murphy et al. (2019)	O'Meara et al. (2015, 2017)

Table 2.1 summarizes the QSO spectra data that is available to us. At high redshift, we have the publicly available HIRES (High Resolution Echelle Spectrometer) QSO spectra taken from the Keck Observatory Archive and UVES (Ultraviolet and Visual Echelle Spectrograph) QSO spectra from the ESO (European Southern Observatory) Archive. We will use suitable HIRES spectra from the KODIAQ (Keck Observatory Database of Ionized Absorption toward Quasars) project (O'Meara et al., 2015) and UVES spectra from the SQUAD (Spectra Quasar Absorption Database) project (Murphy et al., 2019). At low redshift, we also have ~ 500 HST/COS spectra publicly available from the HSLA (Hubble Spectra Legacy Archive) project (Peeples et al., 2017). Although the majority of these QSO spectra are taken to study Damped Lyman α (DLA) systems, many sightlines provide a long wavelength coverage sufficient for our analysis. So far we have data from analysis of ~ 100 spectra. For ground-based telescopes (VLT and Keck) information on Ly α absorbers in the spectra of the QSOs is restricted by the atmospheric cutoff at $\sim 3050 \text{ \AA}$, meaning that absorbers at $z \leq 1.5$ can not be detected from the ground. At the HIRES and UVES resolution of $\sim 7 \text{ km s}^{-1}$, HI is fully resolved and among metal absorption lines CIV and SiIV lines are resolved so that a reliable absorption line parameter can be obtained using profile fitting via the code VPFIT (Section 2.2.4).

2.2 Line Profile Analysis

In high resolution spectra ($\text{FWHM} < 25 \text{ kms}^{-1}$), it is possible to resolve individual absorption lines in the Ly- α forest. This section will discuss the theory and methods used for our absorption line profile analysis.

2.2.1 Optical Depth

The optical depth (τ) is a measure of the absorption strength at a specific wavelength and is fundamental to understanding the absorption features in the Ly α forest. In the context of absorption lines, optical depth quantifies the likelihood that photons are absorbed as they pass through an absorbing medium—in this case, neutral hydrogen in the IGM.

As shown in Figure 2.1, consider a beam of light of wavelength near to that of Ly α , with an initial intensity I_0 , passing through a homogeneous cloud with neutral hydrogen (HI) number density n_{HI} . Let us assume that the cross-section of a single HI atom is σ . In reality, this cross-section will be more like a probability distribution of the electron cloud around the nucleus. When the light travels through an infinitesimal distance of dl , the change in intensity would be,

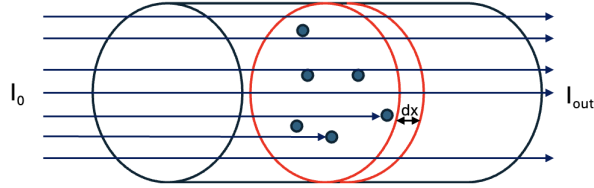


Figure 2.1 A beam of light passing through a cylinder of absorbers. Photon gets absorbed as it hits an absorber.

$$dI = -I_0 n_{\text{HI}} \sigma dl. \quad (2.1)$$

We define

$$d\tau \equiv n_{\text{HI}} \sigma dl. \quad (2.2)$$

Then, integrating eq.2.1 along the path of the light gives us

$$I_{\text{out}} = I_0 e^{-\tau} \quad (2.3)$$

As optical depth gets larger, the amount of light transmitted drops exponentially. When $\tau < 1$, the gas is considered to be optically thin or transparent and when $\tau \gg 1$, the gas is considered to be optically thick, or opaque.

2.2.2 Line Broadening

Ideally, spectral absorption lines occur at the resonant frequency, where the frequency is related to the energy difference between the two energy states of the electron via

$$(E_i - E_f) = h\nu. \quad (2.4)$$

However, in reality the absorption (or emission) lines are never monochromatic in observations. There are several reasons for this. A few common line broadening mechanisms outlined below are: natural line broadening, Doppler broadening, collision broadening and instrumental broadening.

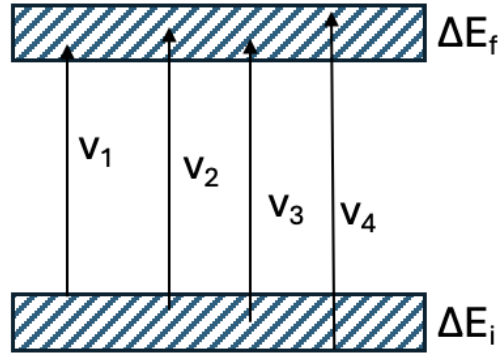


Figure 2.2 Visualization of uncertainty in ν from Heisenberg's uncertainty principle.

Natural broadening of an absorption line profile originates from Heisenberg's uncertainty principle:

$$\Delta E \Delta t \geq \hbar/2, \quad (2.5)$$

where ΔE is the uncertainty in the energy of the state and Δt is the uncertainty in the occupation time of the state (\propto half-life). Due to this the absorption line spreads from looking like a Dirac delta function to a line profile with a shape given by a Lorentzian distribution of the form:

$$L(\nu) = \frac{\Delta\nu_N/2}{(\nu - \nu_0)^2 + (\Delta\nu_N/2)^2}, \quad (2.6)$$

where ν_0 is the resonant frequency of the transition and $\Delta\nu_N = 2\pi/t_{1/2}$ is called the natural line width corresponding to that transition. Eq. 2.6 can be derived by considering the electron-proton system as a classical damped harmonic oscillator in the small damping regime ($\Delta\nu_N \ll \nu_0$).

Another source of absorption line broadening is the thermal/Doppler broadening which originates from the temperature of a gas cloud. At a temperature T, the thermal velocities

of individual gas particles follow the Maxwell-Boltzmann distribution. Hence the thermal velocity dispersion is

$$v_{\text{th}} = \sqrt{\frac{2k_B T}{m}}, \quad (2.7)$$

where k_B is the Boltzmann constant, and m is the mass of an individual gas atom. This distribution in velocity also means that the absorption line from the gas cloud will be smoothed due to Doppler shift. So, the line width associated with the Doppler broadening would be

$$\Delta\nu_D = \frac{v_{\text{th}}}{c} \nu_0. \quad (2.8)$$

We write the expression for line profile broadening in terms of this Doppler width($\Delta\nu_D$) as

$$G(\nu) = \frac{1}{\sqrt{\pi}} e^{-(\frac{\nu-\nu_0}{\Delta\nu_D})^2} \quad (2.9)$$

Apart from the two processes above, observed absorption lines can be further smoothed by collisions and turbulence in the gas, as well as by the line spread function (LSF) of the instrument itself. The latter can be easily accounted for by knowing the LSF of the instrument in a controlled environment.

Line widths from collisions, again follows a Lorentzian profile since the inelastic collisions can be seen as changes in energy states as in the case of natural broadening. So to the total width of the Lorentzian profile due to both of these factors would be

$$\Delta\nu_L = \Delta\nu_N + \Delta\nu_{\text{coll}}. \quad (2.10)$$

Meanwhile, depending on the velocity distribution, the smoothing due to turbulence can be either Gaussian or non-Gaussian. Since the actual mechanism of the turbulence is not understood in detail, any excess spread in the absorption line width is attributed to non-thermal processes through a single parameter (discussed in 2.2.4).

2.2.3 Voigt Profile

Accounting for the factors in the previous subsection, the overall profile of an absorption line would be a combination of the Lorentzian and the Gaussian profiles. This is given by the Voigt profile, named after a German physicist Woldemar Voigt.

First, for simplification, we define the following variable:

$$x \equiv \frac{\nu - \nu_0}{\Delta\nu_D}, \quad (2.11)$$

and the parameter:

$$a \equiv \frac{\Delta\nu_L}{2\Delta\nu_D}. \quad (2.12)$$

So, equations 2.6 and 2.9 become

$$G(x) = \frac{1}{\sqrt{\pi}} e^{x^2}, \quad (2.13)$$

and

$$L(x) = \frac{a}{\pi} \frac{1}{x^2 + a^2}. \quad (2.14)$$

The Voigt profile, then, is defined as the convolution of the Lorentzian and the Gaussian:

$$V(x) = \int_{-\infty}^{\infty} L(x-y)G(y)dy = \frac{1}{\sqrt{\pi}\Delta\nu_D} H(a, x), \quad (2.15)$$

where

$$H(a, x) = \frac{a}{\pi} \int_{-\infty}^{\infty} \frac{e^{-y^2}}{(x-y)^2 + a^2} dy \quad (2.16)$$

is the Voigt-Hjerting function (Hjerting, 1938). Eq. 2.15 gives the overall normalized line profile of an absorption line. To get the absorption cross-section (eq.2.2), we need to multiply it by a proportionality constant which can be derived from dispersion theory of electromagnetic waves in an absorbing medium. Then we will have,

$$\sigma_x = \frac{\pi e^2}{m_e c} f V(x) \quad (2.17)$$

or,

$$\sigma_x = f \frac{\sqrt{\pi} e^2}{m_e c \Delta\nu_D} H(a, x), \quad (2.18)$$

where f is known as the oscillator strength or the probability of occurrence of the transition. Finally we can replace σ in eq.2.2 and get the Ly- α optical depth,

$$\tau_{\text{Ly}\alpha} = f_{\text{Ly}\alpha} N_{\text{HI}} \frac{\sqrt{\pi} e^2}{m_e c \Delta\nu_D} H(a, x), \quad (2.19)$$

where $N_{\text{HI}} = \int n_{\text{HI}} dl$ is the column density of neutral hydrogen integrated along the line of sight. This equation is used commonly for fitting absorption lines with Voigt profiles, characterizing each absorber by the column density and the line width. The resultant profile combine properties of both Lorentzian and Gaussian profiles as shown in Figure 2.3.

2.2.4 VPFIT: Voigt Profile Fitting for Absorption Line Analysis

To analyze the Lyman-alpha forest and other absorption features in quasar spectra, we use **VPFIT**, a Voigt profile fitting software developed by Carswell and Webb (2014). **VPFIT** is widely adopted for precision analysis of absorption lines. **VPFIT** allows us to decompose complex absorption spectra into individual Voigt profiles, which describe the shape of absorption lines due to a combination of Doppler and natural broadening effects. By fitting these profiles, we can determine the physical properties of the gas along the line of sight, such as column densities, temperatures, and turbulent velocities, enabling detailed comparisons between simulated and observed spectra.

VPFIT iteratively adjusts parameters such as the central wavelength, column density, and Doppler broadening parameter until it finds an optimal fit for each absorption feature.

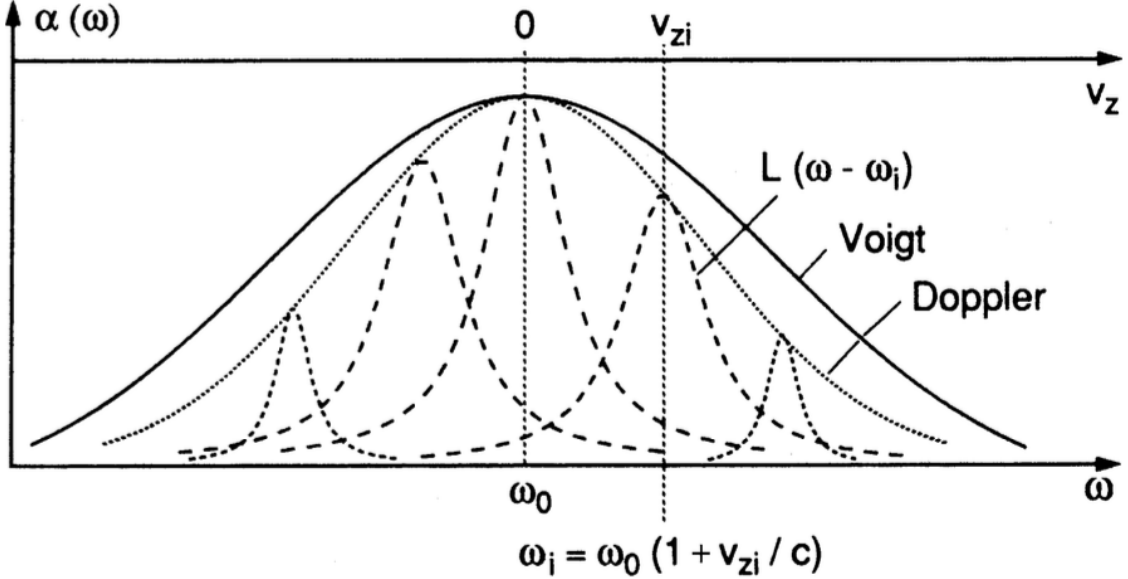


Figure 2.3 A visualization of the Voigt profile as a combination of a Lorentzian and Gaussian Profile. *Credits: Demtröder (2008).*

This process enables the precise extraction of gas properties from each fitted line. The key parameters obtained through **VPFIT** fitting include:

- **Column Density (N_{HI}):** Represents the amount of neutral hydrogen along the line of sight for each absorption feature. The usual unit for column density fits from **VPFIT** is $\log_{10}(N_{\text{HI}}/\text{cm}^{-2})$.

- **Doppler Parameter (b):** A measure of the line width, which can indicate thermal motion (temperature) and small-scale turbulence within the absorbing gas. The unit of b from **VPFIT** is in km s^{-1} and is given by eq. 2.7 plus any width contribution from non-thermal motion.

$$b = \sqrt{\frac{2k_B T}{m_X} + b_{\text{non-thermal}}^2} \quad (2.20)$$

Note that the contribution of non-thermal motion to the line width can be found if we fit absorption lines of two different species (e.g., HI and CIV) coming from the same gas cloud assuming that both species are at the same temperature and have the same non-thermal velocity distribution within that gas cloud.

- **Redshift (z):** The redshift of each absorption feature reveals the relative velocity and distance of the gas, allowing for the reconstruction of large-scale structure along the sightline.

An example of fitted absorption lines can be seen in Figure 2.4. For this project, **VPFIT** is applied to synthetic spectra generated from cosmological simulations, as well as to observational spectra of quasars. By comparing the fitted column densities and Doppler pa-

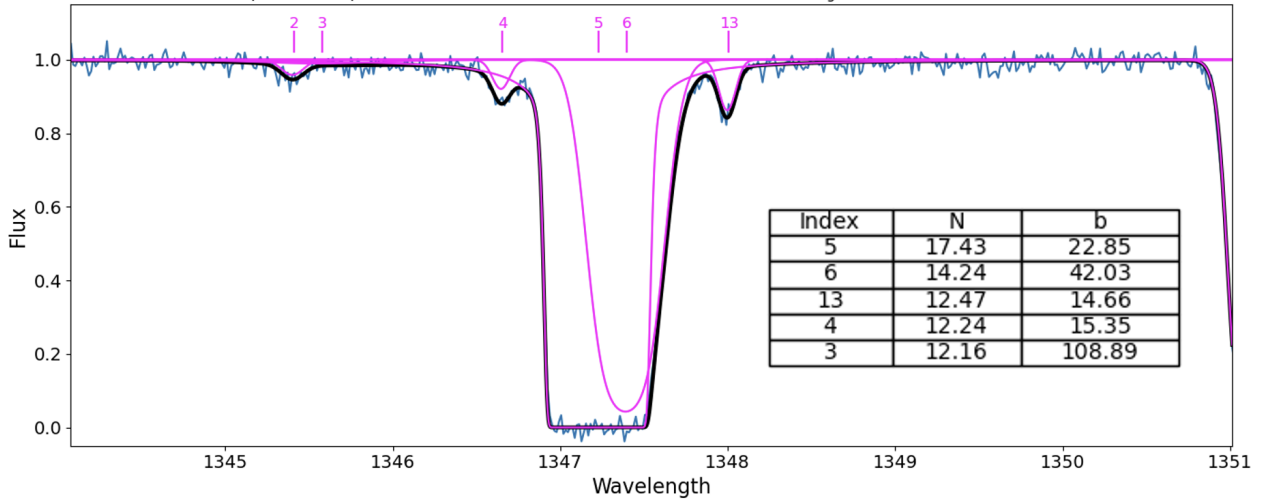


Figure 2.4 Absorption lines in a spectra fitted using **VPFIT**. The magenta lines indicate individual profiles and the black line is the combined profile after adding all the individual absorption lines. The table on the right gives the best fit parameters of N_{HI} and b values each absorption line in the figure.

rameters in both datasets, we aim to assess how well the simulations replicate the observed properties of the IGM and the CGM.

While **VPFIT** provides highly accurate fits to absorption lines, there are uncertainties associated with the decomposition of blended lines, especially in regions with saturated absorption. These uncertainties can affect the inferred column densities and temperatures, potentially biasing comparisons between simulations and observations. To mitigate these effects, this study includes error analysis on fitted parameters and cross-checks with alternative fitting techniques when possible.

2.3 Cosmological Simulations to be Analyzed during this PhD Thesis

The core of this research involves the use of large-scale cosmological simulations to study the CGM and its relationship with galaxies. Two primary simulations are employed: the Sherwood simulations and the Illustris-TNG simulation suite, described below. Both simulations model the formation and evolution of structures in the universe, but with different emphases on physical processes and resolutions.

2.3.1 The Sherwood Simulations

The Sherwood Simulation suite (Bolton et al., 2017) is a collection of high resolution hydrodynamical simulations to study the diffuse gas in the universe. The simulations are performed at different resolutions, and of particular interest for this thesis, implement a variety of feedback physics including models for galactic outflows such as stellar wind and

AGN feedback. Table 2.2 lists the simulations which are currently being used in our work; further entries will be added as our work progresses.

The simulations are based on the code P-GADGET-3 with modifications applied for different physics for different simulation boxes. P-GADGET-3 is a Tree-PM SPH code and it is an updated and extended version of the publicly available code GADGET-2 (Galaxies with dark matter and gas interact) published in Springel (2005). The cosmological parameters used in the models is obtained from Planck Collaboration et al. (2014), where $\Omega_m = 0.308$, $\Omega_\Lambda = 0.692$, $h = 0.678$, $\Omega_b = 0.0482$, $\sigma_8 = 0.829$, and $n = 0.961$.¹ A primordial helium fraction of $Y_p = 0.24$ is assumed. The initial conditions are generated at the redshift of $z = 99$ on a regular grid using transfer functions generated by CAMB (Code of Anisotropies in Microwave background; Lewis et al. (2000)). The SPH parameters are $N_{\text{nb}} = 64$ and $l_{\text{soft}} = 1/25^{\text{th}}$ of mean inter-particle spacing ($\sim 1 - 2 \text{ h}^{-1}\text{cMpc}$).

The simulations used in this project (Table 2.2) are performed in two different box sizes: $40 \text{ h}^{-1}\text{cMpc}$ and $60 \text{ h}^{-1}\text{cMpc}$, with the smaller ones having higher resolution than the larger ones. The $60 \text{ h}^{-1}\text{cMpc}$ boxes have four variants of subgrid physics and have outputs at $z < 2.6$, while the $40 \text{ h}^{-1}\text{cMpc}$ boxes have only two variants of subgrid physics and have outputs at $z > 2$. At each resolution we have a “**no feedback**” variant, which does not implement any subgrid physics. In these runs, gas particles with temperature $T < 10^5 \text{ K}$ and overdensity $\Delta (= \rho / \rho_{\text{crit}}) > 10^3$ are converted into collisionless star particles.² On the other hand, the runs with subgrid physics are: “**Only stellar wind**”, “**Stellar wind + AGN feedback**”, and “**Stellar wind + Strong AGN feedback**”. For the higher resolution boxes, the only run with subgrid physics is the Stellar Wind + AGN run. The boxes of the same size have the same initial conditions, and hence have the same large scale structures for one to one comparison.

The Wind Model

The subgrid physics models used in these simulations are taken from the model S15 in (Puchwein and Springel, 2013). The velocity of the wind coming out of a galaxy is taken to be directly proportional to the escape velocity of the galaxy:

$$v_w = \kappa \times v_{\text{esc}}, \quad (2.21)$$

where $\kappa = 0.6$ is the constant of proportionality which fits best with the observations. The escape velocity v_{esc} of the galaxies is calculated assuming a Navarro-Frenk-White (NFW)

¹ $\Omega_m, \Omega_\Lambda, \Omega_b$ are the fractional density of matter, cosmological constant, baryons in the current Universe respectively.

h is the reduced hubble constant,

σ_8 is the matter density fluctuation on scales of $8h^{-1}\text{Mpc}$, and

n is the scalar spectral index of the primordial power spectrum.

² $\rho_{\text{crit}}(z) = \frac{3H^2(z)}{8\pi G}$ is the critical density of the universe at redshift z .

Table 2.2. List of Simulations Analyzed from the Sherwood simulation suite

Model	L_{box} (h^{-1}cMpc)	N_{part}	M_{gas} (M_{\odot})	z (Snapshots Used)	Comments
No feedback	60	2×768^3	6.38×10^6	0.1, 0.3, 2.2, 2.4	Model H02 from Bolton et al. (2022)
wind+AGN	60	2×768^3	6.38×10^6	0.1, 0.3, 2.2, 2.4	Model AGN from Bolton et al. (2022)
wind+strongAGN	60	2×768^3	6.38×10^6	0.1, 0.3, 2.2, 2.4	Model StrongAGN from Bolton et al. (2022)
Only wind	60	2×768^3	6.38×10^6	0.1, 0.3, 2.2, 2.4	Same as wind+AGN, but AGN feedback turned off
No feedback_hires	40	2×1024^3	7.97×10^5	2.2, 2.4, 3.6	Model from Puchwein et al. (2022) (same as No feedback but higher resolution)
wind+AGN_hires	40	2×1024^3	7.97×10^5	2.2, 2.4, 3.6	Same as wind+AGN, but higher resolution

profile for the halos:

$$v_{\text{esc}} = v_{200c} \sqrt{\frac{2c}{\ln(1+c) - c/(1+c)}}, \quad (2.22)$$

with

$$c \equiv r_s/r_{200c} \quad (2.23)$$

and

$$v_{200c} = \sqrt{GM_{200c}/r_{200c}} \quad (2.24)$$

where c is the concentration parameter of the halo, r_s is the NFW scale radius, r_{200c} is the radius at which the mean enclosed density of the halo is $200\rho_{\text{crit}}$, M_{200c} is the total mass enclosed by r_{200c} , and v_{200c} is the circular velocity at r_{200c} .

The amount of gas entering into the wind is taken from Springel and Hernquist (2003), where the energy available for the wind particles is proportional to the star formation rate (\dot{M}_*) and supernova fraction (ϵ_{SN}):

$$\frac{1}{2}\dot{M}_w v_w^2 \propto \epsilon_{\text{SN}} \dot{M}_* \quad (2.25)$$

In galactic wind models, the mass loading factor defined by $\eta \equiv \dot{M}_w/\dot{M}_*$ is of particular importance. In our case, where the galactic winds are driven by energy, the mass loading factor scales as $\eta \sim v_w^{-2}$. So larger halos will have a significantly larger fraction of mass outflows, and thereby suppress star formation to a greater extent compared to smaller halos.

The AGN feedback model

Also taken from Puchwein and Springel (2013), the AGN feedback models seed supermassive blackholes (BHs) of mass $m_{\text{BH,seed}} = 10^4 h^{-1} M_{\odot}$ into the centers of halos when they exceed $5 \times 10^{10} h^{-1} M_{\odot}$. The BH particles are treated as collisionless sink particles that grow with gas accretion and by merging with other BH particles (Sijacki et al., 2007). Two BH particles are merged when they are within their SPH smoothing scale and have velocities smaller than the local sound speed. For simplicity, the BH particles are re-centered to the minimum of the potential well of the halo at every time step.

As mentioned in Chapter 1, the AGN feedback is divided into two modes: ‘quasar mode’ and ‘radio mode’. This is motivated from both theory and observations such as Gallo et al. (2003); Croton et al. (2006). These modes are dependent on the accretion rate of the BH. The accretion rate of a BH particle is calculated using the Bondi-Hoyle-Lyttleton formula:

$$\dot{M}_{\text{BH}} = \frac{4\pi\alpha G^2 M_{\text{BH}}^2 \rho}{(c_s^2 + v^2)^{3/2}}, \quad (2.26)$$

where α is a dimensionless parameter used to boost the accretion rate, ρ is the local density, c_s is the local sound speed of the gas, v is the velocity of the BH relative to the gas ($v = 0$ in our case). An upper limit for the accretion is also imposed in the simulations to be equal to the Eddington limit:

$$\dot{M}_{\text{Edd}} = \frac{4\pi GM_{\text{BH}} m_p}{\epsilon_r \sigma_T c}, \quad (2.27)$$

where m_p is the proton mass, σ_T is the Thompson cross-section and ϵ_r is the radiative efficiency assumed to be equal to 0.1.

The quasar mode is active when the accretion rates are high ($\dot{M}_{\text{BH}} > 0.01 \times \dot{M}_{\text{Edd}}$). In this regime, BHs accrete efficiently and power luminous quasar activity where only a very small fraction of the luminosity thermally couples to the surrounding medium. In both wind+AGN and wind+strongAGN models 0.5 per cent of the accreted rest mass energy is thermally coupled to the surrounding gas.

At lower accretion rates ($\dot{M}_{\text{BH}} < 0.01 \times \dot{M}_{\text{Edd}}$), AGN heating happens through radiatively inefficient feedback in a mostly mechanical form. This is realized in the simulation by injecting bubbles into the host galaxy/cluster triggered by a fractional increase in the BH mass. In the wind+AGN model, a fractional increase (δM_{BH}) in the black hole mass of 10^4 , with 2% of the rest mass energy used for injecting hot AGN bubbles. Whereas, for the wind+strongAGN model, δM_{BH} is increased to 10^{-2} , with 8% energy being used to inject AGN bubbles. This leads to a less frequent but stronger bubble injection, resulting in significantly less gas fraction nearby halos.

2.3.2 The IllustrisTNG Simulations

The IllustrisTNG (The Next Generation) simulation suite (Springel et al., 2018) is a set of state-of-the-art cosmological hydrodynamical simulations designed to model accurate subgrid physics. This suite builds on the original Illustris project (Vogelsberger et al., 2014), with updates in feedback physics, improved resolution, and a refined cosmological model. Table 2.3 lists the specific IllustrisTNG simulations used in this project, detailing the box sizes, resolution, and available redshift snapshots.

The simulations are performed using the AREPO code (Weinberger et al., 2020), a moving-mesh hydrodynamics solver that combines the strengths of SPH and traditional grid-based methods. AREPO’s moving-mesh approach provides greater accuracy in modeling gas dynamics across a wide range of densities, making it particularly effective for

Table 2.3. The IllustrisTNG Simulation Suite

Model	L_{box} (h^{-1}cMpc)	N_{part}	M_{gas} (M_{\odot})	M_{DM} (M_{\odot})
TNG50	35	2×2160^3	8.5×10^4	4.5×10^5
TNG100	75	2×1820^3	1.4×10^6	7.5×10^6
TNG300	205	2×2500^3	1.1×10^7	5.9×10^7

capturing the details of turbulence and shocks on smaller scales. All runs in the IllustrisTNG suite employ cosmological parameters from Planck Collaboration et al. (2016), with $\Omega_m = 0.31$, $\Omega_{\Lambda} = 0.69$, $h = 0.677$, $\Omega_b = 0.0486$, $\sigma_8 = 0.8159$, and $n_s = 0.97$.

Box Sizes, Resolution, and Redshift Coverage

The IllustrisTNG suite includes three main box sizes—TNG50, TNG100, and TNG300—which vary in both volume and resolution. These boxes cover a range of cosmic scales, enabling studies of everything from detailed galaxy evolution to large-scale cosmic web structure:

1. **TNG50**: This box spans 50 Mpc per side and has the highest resolution, with particle masses of $8.5 \times 10^4 M_{\odot}$ for baryons. It is ideal for detailed studies of small-scale galactic structures and CGM properties, particularly at low redshifts.
2. **TNG100**: Spanning 100 Mpc per side, this intermediate-resolution box provides a balance between computational efficiency and physical detail, with baryonic particle masses of $1.4 \times 10^6 M_{\odot}$. TNG100 is well-suited for studying galaxy evolution and CGM dynamics across a range of redshifts.
3. **TNG300**: The largest box, at 300 Mpc per side, TNG300 is optimized for capturing large-scale structure and the evolution of massive galaxy clusters. With baryonic particle masses of $1.1 \times 10^7 M_{\odot}$, it is less detailed on small scales but highly effective for large-scale statistical studies.

Each of these runs includes a total of 100 snapshots³ in the redshift range of $0 \leq z \leq 20$, allowing for evolutionary studies from early times up to the present day. This broad redshift coverage is essential for analyzing how the CGM and IGM evolve in response to galactic feedback processes over cosmic time.

Subgrid Physics Models

IllustrisTNG incorporates a range of subgrid models that capture critical astrophysical processes, including star formation, stellar feedback, black hole growth, and AGN feedback.

³A snapshot is defined as all the data of a simulation box at a specific redshift.

These models are designed to reproduce observed properties of galaxies, such as their stellar mass, gas content, and metallicity.

1. Stellar Feedback: Instead of scaling the wind velocity with the escape velocity, the TNG suite implements the stellar feedback model where v_w scales with the local, one-dimensional DM velocity dispersion (σ_{DM}). They also set a minimum wind velocity injection $v_{w,\text{min}} = 350 \text{ km s}^{-1}$:

$$v_w = \max \left[7.4 \times \sigma_{\text{DM}} \left(\frac{H_0}{H(z)} \right)^{1/3}, v_{w,\text{min}} \right], \quad (2.28)$$

where H_0 and $H(z)$ are the present day Hubble constant and the Hubble parameter at redshift z respectively. More details can be found in Vogelsberger et al. (2013) and Pillepich et al. (2017).

2. Black Hole Accretion and Feedback: In TNG, BH particles of mass $8 \times 10^5 h^{-1} M_\odot$ are seeded into halos above the mass $5 \times 10^{10} h^{-1} M_\odot$. The accretion rates are calculated using 2.26, but without the boosting factor α . Similar to Sherwood, TNG also implements AGN feedback in two different modes. The accretion rate threshold for differentiating between high/low accretion mode now scales with the BH mass,

$$\chi = \min \left[\chi_0 \left(\frac{M_{\text{BH}}}{10^8 M_\odot} \right)^\beta, 0.1 \right], \quad (2.29)$$

where $\beta = 2.0$ and $\chi_0 = 0.002$.

In high accretion quasar mode 2% of the rest mass energy of the accreted gas is injected into the gas surrounding the BH in the form thermal energy. In the low accretion mode, a kinetic BH-driven wind is implemented in place of the bubble model. In this mode, the energy is injected into wind particles as pure kinetic energy instead of thermal energy. The fraction of energy injected this way is kept at < 2%, however this is also density dependent to make sure that such winds do not drive the gas density to an unrealistically low values in low density halos. More details can be found in Weinberger et al. (2017).

3. Magnetic Fields and Other Subgrid Physics: IllustrisTNG is one of the first large-scale cosmological simulations to include a full magnetohydrodynamic (MHD) treatment, allowing for the evolution of cosmic magnetic fields. This addition enables a more realistic model of gas dynamics and pressure support in the CGM, particularly in dense regions around galaxies.

IllustrisTNG also includes detailed models for radiative cooling, including metal-line cooling and photoionization by a uniform UV background (Haardt and Madau, 2012). The metal enrichment model tracks multiple species (e.g., Fe, O, C) produced by supernovae and stellar winds, enriching the gas over time. This enriched gas can cool more efficiently, influencing the formation of subsequent generations of stars and altering the CGM's thermal properties.

Although only one kind of subgrid physics model is applied in all the simulation runs, the richness of the physics and large redshift coverage make IllustrisTNG a versatile

tool for studying the CGM and IGM. TNG50’s high resolution allows for detailed studies of small-scale CGM structure, while TNG100 and TNG300 provide a statistical approach to large-scale structure and galaxy evolution. By comparing results across different runs, it is possible to analyze how stellar and AGN feedback influence gas properties, metallicity, and density in the CGM over cosmic time, providing insights into the relationship between galaxies and their gaseous halos. For comparison with the 60cMpc boxes of Sherwood, we will mainly focus on the simulation TNG100 (75cMpc) in this project.

2.4 Simulation Data Analysis

We analyze the simulation data with two approaches. First, to compare the Ly α forest statistics in observation, we shoot lines of sight (LOSs) across the simulation boxes at thousands of random locations. We obtain several physical properties of the gas along these LOSs such as density, temperature, metallicity, HI fraction, peculiar velocity, etc. Most importantly, we also obtain the optical depth for different absorption lines along the LOS. From the optical depth, we create thousands of mock spectra which would be equivalent to QSO spectra in observations. The second approach focuses more on the halos, where we target specific isolated galaxies and look at the properties of these targets at different redshifts.

2.4.1 Mock Spectra from Simulation

The method for extracting LOS spectra from the simulation boxes follows from Theuns et al. (1998). We divide the LOS into bins of $n_{\text{pix}} = 2048$ pixels of width Δ along the sightline. Using eq. 1.2, with a weight factor indicating the fractional abundance of the species (HI fraction for Ly α), we compute the density ρ_X , density-weighted temperature $(\rho T)_X$ and density-weighted velocity $(\rho v)_X$ at each bin. Once we have these values, we calculate the optical depth in each bin by using eq. 2.19. We convert eq. 2.19 to wavelength space from frequency space for convenience:

$$\tau_\lambda = \sigma_\alpha \frac{c N_X}{\sqrt{\pi} \Delta \lambda_D} H(a, x), \quad (2.30)$$

where σ_α is the cross-section, $N_X = \rho_X \Delta$ is the column density of the species, and $\Delta \lambda_D$ is the Doppler width of the species in wavelength space with the temperature information inside.

For Ly α , the cross-section is $\sigma_\alpha = (3\pi\sigma_T/8)^{1/2} f_{\text{Ly}\alpha} \lambda_0 = 4.45 \times 10^{-18} \text{cm}^2$, with oscillator strength $f_{\text{Ly}\alpha} = 0.41615$, the Thomson cross-section $\sigma_T = 6.625 \times 10^{-25} \text{cm}^2$, and the rest wavelength corresponding to resonant frequency of Ly α $\lambda_0 = 1215.67 \text{\AA}$. The calculated optical depth can then be redshifted to the observed wavelength using the relation

$$\lambda = \lambda_0(1+z)(1+v/c), \quad (2.31)$$

where v is the peculiar velocity.

The HI optical depth is then rescaled according the mean observed flux using a power law from Kim et al. (2007)

$$\tau_{\text{HI}}^{\text{eff}} = 0.0023 \pm (1 + z)^{3.65}. \quad (2.32)$$

The optical depth is then converted into flux using eq. 2.3. For a better comparison with the observed spectra, the extracted spectra are convolved with an appropriate LSF ($\text{FWHM} \sim 7 \text{km s}^{-1}$) and a gaussian noise with an appropriate S/N (~ 100). Once all the post-processing steps are done, the spectra are fitted using VPFIT as described in Section 2.2.4.

2.4.2 Individual Galaxy halos in Simulation

To investigate the CGM around galaxies, we look at halos of isolated galaxies in different mass ranges. For IllustrisTNG, we do this using the publicly available Group and Subhalo catalogues which are obtained using the Subfind algorithm (Springel et al., 2001). A merger tree of subhalos for each simulation run is also available using which each galaxy can be tracked at different snapshots. For the Sherwood simulations, we run the ROCKSTAR (Robust Overdensity Calculation using K-Space Topologically Adaptive Refinement) halo finder algorithm (see Behroozi et al. (2013) for more details) on all the available snapshots. Obtaining a merger-tree is not possible since the available snapshots are too far apart in time. So a halo is tracked in a different snapshot by searching for a halo with appropriate mass ratio (given the approximate growth rate of structure) inside an appropriate region along with visual inspection.

In the next Chapter, we discuss the results we have obtained so far using the methods described in Chapter 2.

CHAPTER 3

PRELIMINARY RESULTS AND DISCUSSION

So far, we have been analyzing the simulation boxes at two redshifts: $z=0.1$ and $z=2.4$, considering only the TNG100-1 and Sherwood 60cMpc simulations. In this chapter, we discuss our preliminary findings from our analysis.

3.1 Individual Halo Analysis

We start by looking at the properties of the gas around the same halo in different feedback regimes. For this we make 2-D projected plots of gas density, temperature, HI column density, etc. in the regions around halos to visually investigate any differences.

To do this, we first obtain the halo catalogues of all the simulation boxes either using the Illustris API for TNG or running ROCKSTAR on the Sherwood snapshots. Once we have the halo catalogues, we bin the halos according to their mass in several bins such as $10^{10.75} - 10^{11.25}$, $10^{11.75} - 10^{12.25}$, $10^{12.75} - 10^{13.25} M_{\odot}$, etc. Since our project focuses on the cold CGM, we avoid halos hosting groups/clusters of galaxies. Such halos host hot gas ($T > 10^6 K$) in the ICM which we cannot observe in the Ly α forest. Soft X-ray telescopes/spectroscopes are needed to observe such gas. Keeping this in mind, we search for isolated galaxies. This is done by comparing the mass of the halo to any other satellite halo nearby. If no other halo of significant mass is present within an appropriate distance, i.e., no massive substructure is present within the galaxy halo, we select that halo for our analysis.

3.1.1 Gas Density

In Figure 3.1, we show the projected gas density of a halo in different feedback physics. The upper panels shows a halo of mass $\sim 10^{11} M_{\odot}$ and the lower panels show a halo of mass $\sim 10^{12} M_{\odot}$. Note that the two halos in the upper and lower panel are different as we are still trying to figure out the best way to track a halo in different snapshots since the snapshots available from Sherwood simulations are far apart, unlike TNG.

At $z=2.4$, we do see a difference in gas mass in the halo in the No feedback run compared to the run with subgrid physics. This is because without any outflows, star formation rate is much higher and the halo runs out of gas very rapidly by forming stars. However, the gas is seem to be insensitive to AGN feedback, as small halos like these do not have a supermassive black hole (SMBH) powerful enough to have an impact on the gas.

In contrast, the halo at $z=0.1$ looks significantly different in each simulation. The halo with no feedback has less gas than the one with only stellar wind due to the reasons mentioned above. However, when AGN feedback is turned on, we see that a substantial amount of gas has escaped to outside of the virial radius (R_{vir}) of the halo. This effect is very prominent in the strong AGN feedback run where virtually no gas is left inside the halo. We will investigate

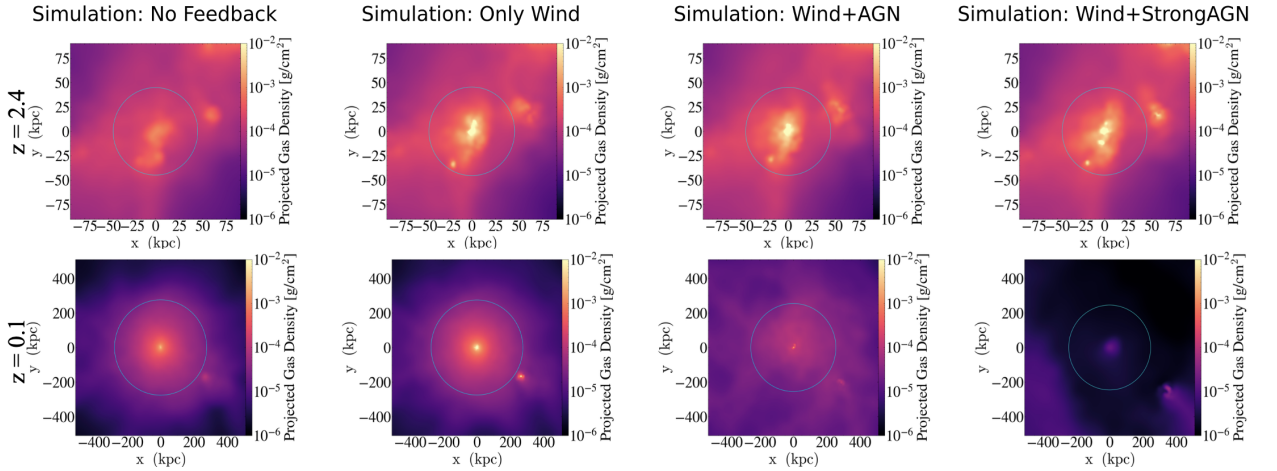


Figure 3.1 Projected gas density of a halo in four different feedback physics of Sherwood simulations. The mass of the halo at $z=2.4$ is $\sim 10^{11} M_{\odot}$, and $z=0.01$ is $\sim 10^{12} M_{\odot}$. The cyan circle represents the virial radius of the dark matter halo. We see that at higher redshifts, AGN feedback is not significantly changing the gas distribution but as we come to lower redshift, the stronger AGN feedback drives almost all of the gas out of the halo region.

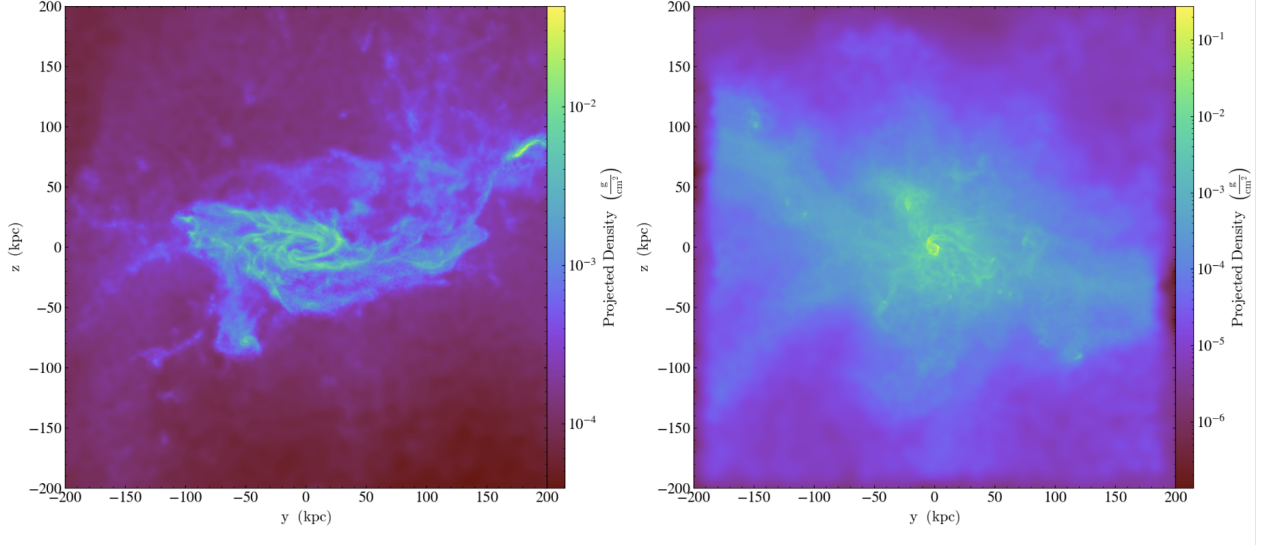


Figure 3.2 Gas density projection of a galaxy of mass $10^{12.38} M_{\odot}$ at $z=0.1$ (left) and $z=2.4$ (right) in TNG100-1.

this effect further, to see if lower redshift CGM observations can be used to constrain the strength of AGN feedback in the universe.

A similar plot for a halo in TNG100-1 as seen in Figure 3.2. With much higher resolution and superior subgrid physics, we can see much finer substructure in the galaxy including the spiral arms. Direct visual comparison with the Sherwood halos is not possible. For

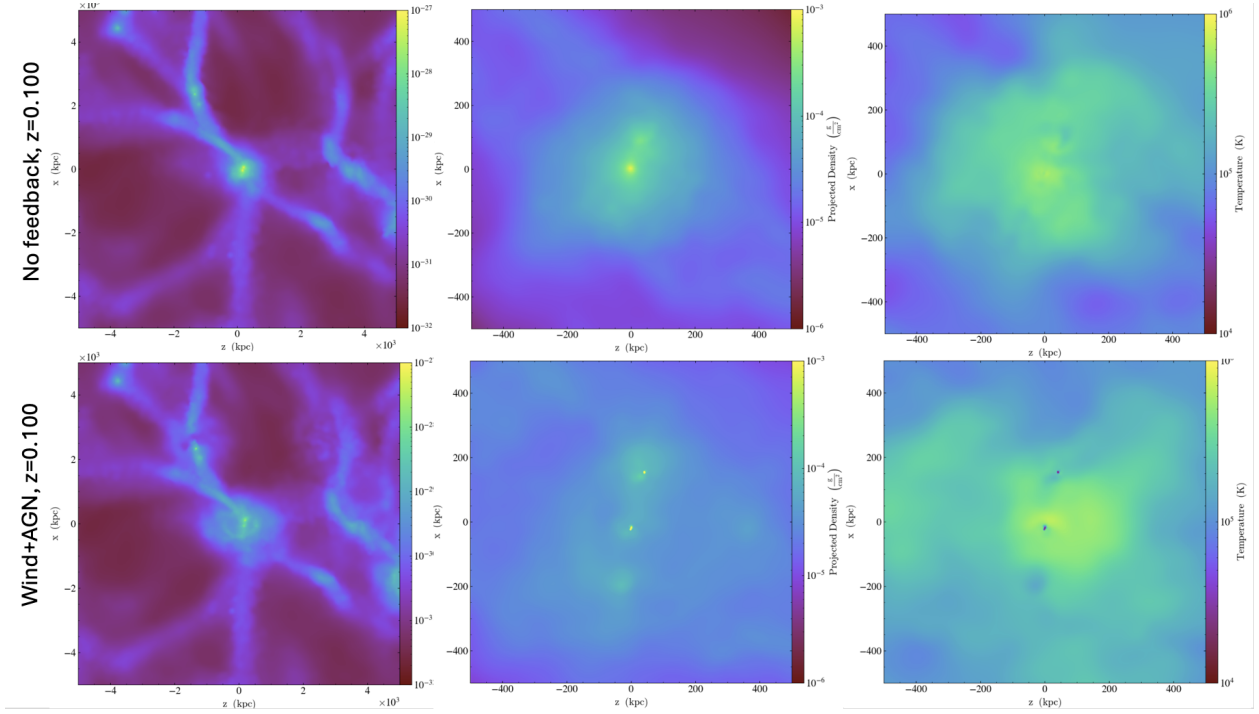


Figure 3.3 *Left:* Projected gas density map of a thin slice centered at the same halo in no feedback and wind+AGN simulation. *Middle:* Zoomed-in projection map of the gas density. *Right:* 2-D temperature map around the halo.

comparison, further analyses such as looking at radial profiles, statistics of several halos in a mass bin needed.

3.1.2 Temperature

We also look at the effect of the feedback process on the gas temperature surrounding halos. The right panels of Fig. 3.3 show the gas temperature of the same halo in no feedback and wind+AGN simulation at $z=0.1$. The difference is more visible further away from the halo where gas temperature is higher with feedback compared to no feedback. Note that the leftmost panels shows the location of the halo in the cosmic web where we can see the gas is more diffuse in the wind+AGN box.

A closer look at the gas temperature is done by filtering out gases in different temperature bins. We plot 2-D gas density of the gas in three temperature bins: $10^{3.5} - 10^4 \text{ K}$, $10^4 - 10^{4.5} \text{ K}$, $10^{4.5} - 10^5 \text{ K}$. In Figure 3.4, see the difference more clearly. In the wind+AGN halo, almost no gas is present in the lowest temperature bin near the center of the halo, while relatively little gas is present in the intermediate bin. In the $10^{4.5} - 10^5 \text{ K}$ bin however, we see more gas, which tells us that AGN feedback is heating up the CGM which could potentially make this gas too ionized to be observable in Ly α absorption.

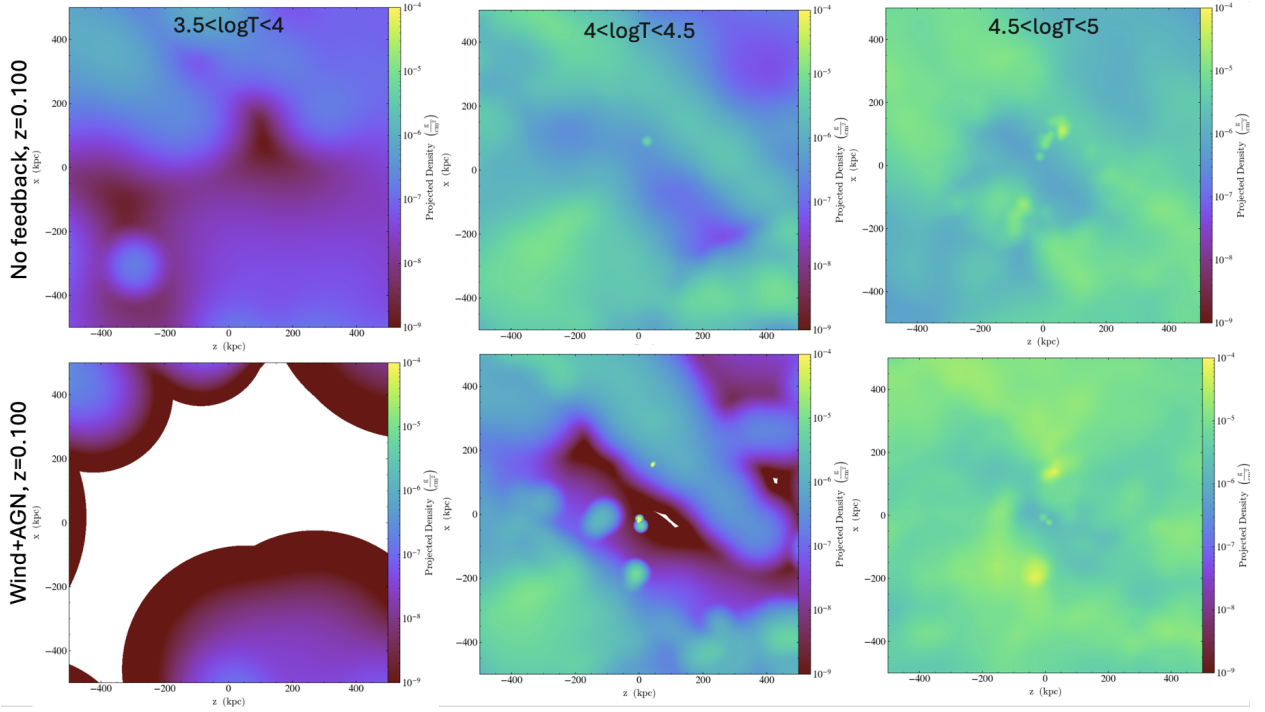


Figure 3.4 Gas density map around the halo in fig. 3.3, in three different temperature bins. The white region implies there is no gas in that temperature bin inside that region.

We also examine the distribution of the gas in the temperature density plane. Fig. 3.5 shows the correlation between temperature and density in the vicinity of the halo in Fig. 3.1 at $z=2.4$. At this redshift, gas is not as hot as the previous example at $z=0.1$. We can clearly see the negative correlation between temperature and density where the densest gas is also the coldest due to radiative cooling. The right hand panels shows the column density of HI which tells us that the gas in the outer CGM should be seen in Ly α absorption. This is shown in figure 3.6, where we shoot an LOS at an impact parameter of $0.75R_{\text{vir}}$. A saturated Ly α absorption line is seen in the extracted spectrum. Targeted LOSs such as this one would be helpful in understanding how CGM should look like in observed QSO spectra. In future, we also plan to look at metal absorption lines coming from these gas clouds by predicting the metal abundance present in the gas clouds using the prescriptions contained in the CLOUDY code (Chatzikos et al., 2023) and calculating optical depths for metal species such as CIV and SIV along the LOS.

3.2 Statistical Analysis

In our statistical approach which is more relevant for comparison with observed data, we shoot thousands of LOSs in each simulation box and extract spectra along them. The details of this method are in section 2.4. So far we have 16384 lines per Sherwood snapshot in Table

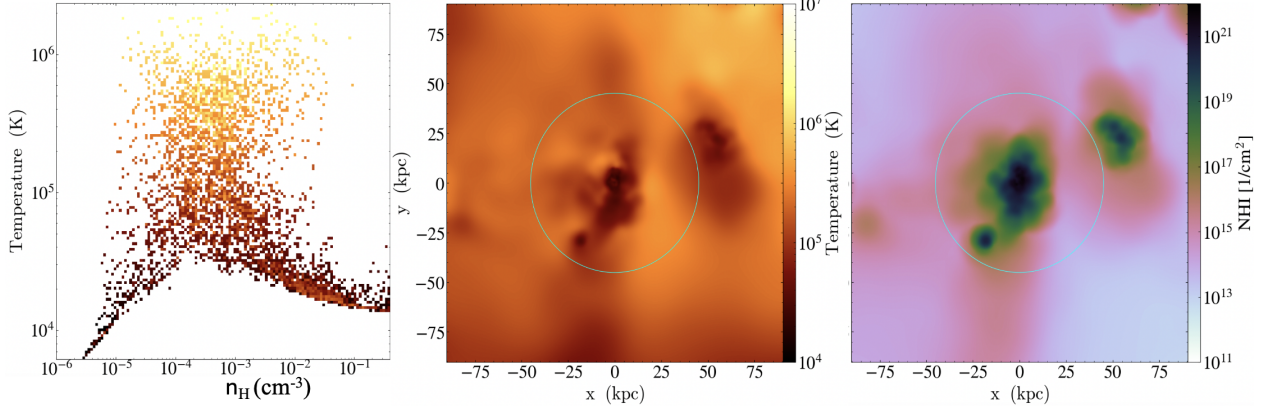


Figure 3.5 *Left*: Distribution of gas particles in the temperature-density plane around the halo in upper panels of Fig. 3.1 in the Sherwood wind+AGN simulation at $z=2.4$. *Middle*: A 2-D projected temperature map of the halo. *Right*: A column density map of the neutral hydrogen in the halo. The negative $T - \rho$ relationship can be clearly seen in all the plots where temperature is coldest at the densest regions.

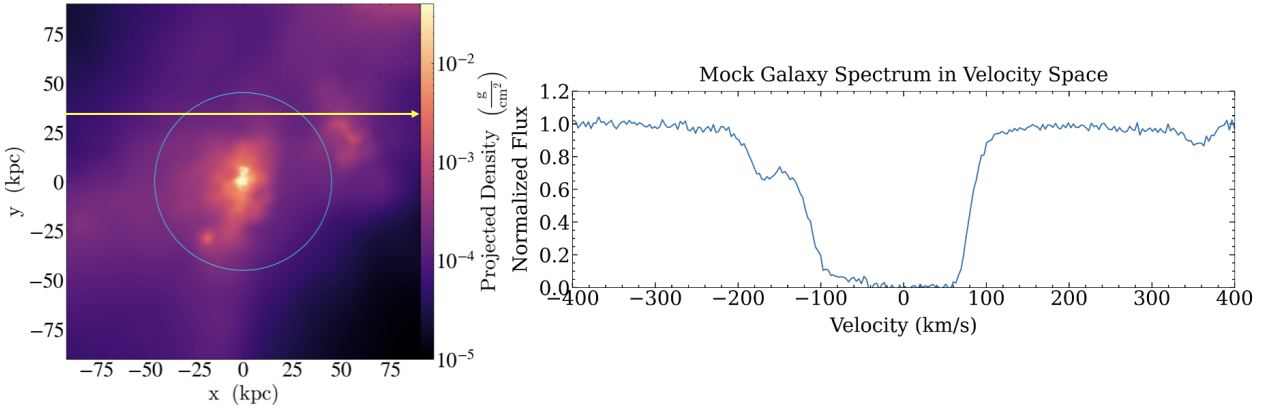


Figure 3.6 An example mock Ly α spectrum extracted from a halo in Sherwood wind+AGN simulation at $z=2.4$. The yellow arrow in the upper panel shows the position and direction of the line of sight with respect to the halo. The LOS has an impact parameter of $0.75R_{\text{vir}}$ from the center of the halo. The absorption line is well saturated as expected from a dense gas cloud in the CGM. This is the same halo shown in Figs. 3.1 and 3.5.

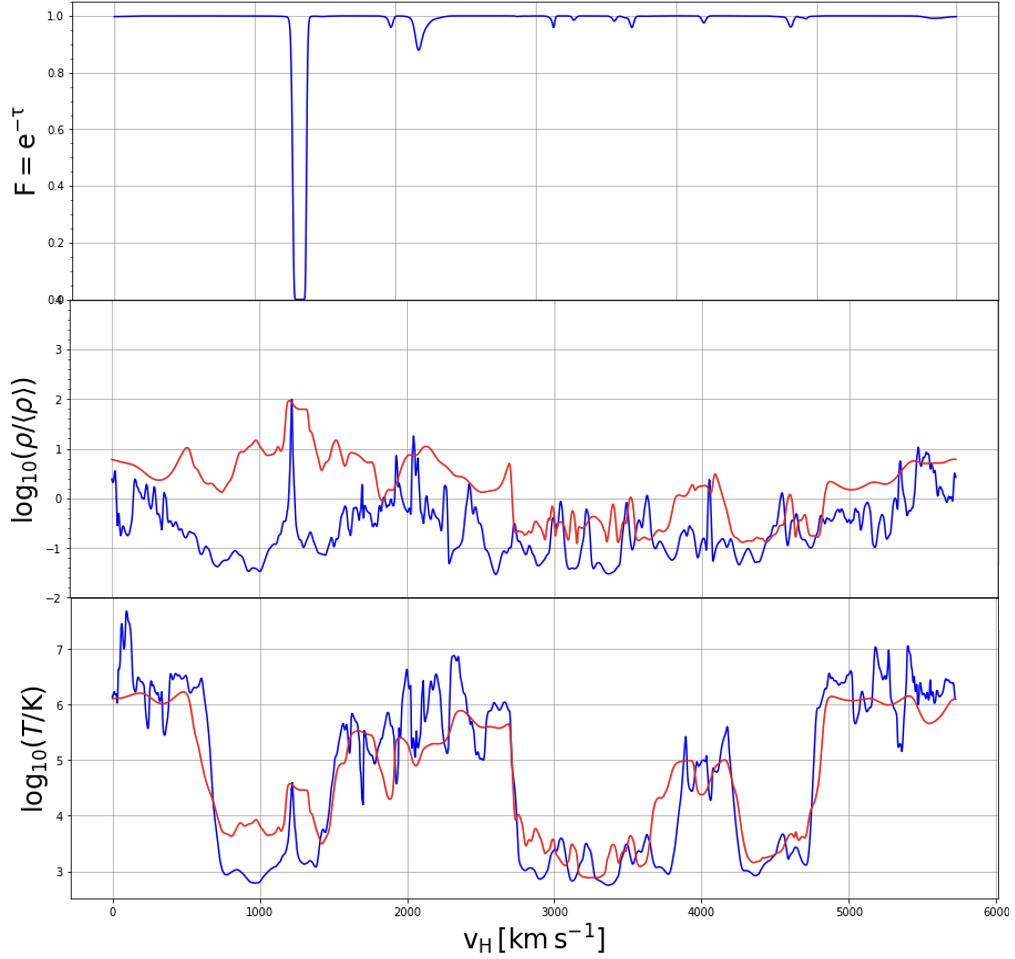


Figure 3.7 *Top*: Raw spectrum of a random line of sight in wind+strongAGN at $z=0.1$.
Middle: Comparison between the volume-weighted density (blue) and optical depth-weighted density (red).
Bottom: Comparison between the volume-weighted temperature (blue) and optical depth-weighted temperature (red).

2.2 readily available as part of on the fly LOS extraction in the Sherwood run. We have also extracted 5000 random LOSs for TNG100-1 at $z=0.1$. These spectra are fitted using the automatic fitting feature in VPFIT which gives us a list of column density and Doppler width b values for all of the absorbers along these LOSs. The temperature and density in the initial LOS file is volume-weighted which is not desirable for studying absorbers in CGM as the values would be dominated by low density (higher volume) regions. So, once we obtain the optical depth, we also compute the optical depth-weighted temperature and density along the LOS (Figure 3.7).

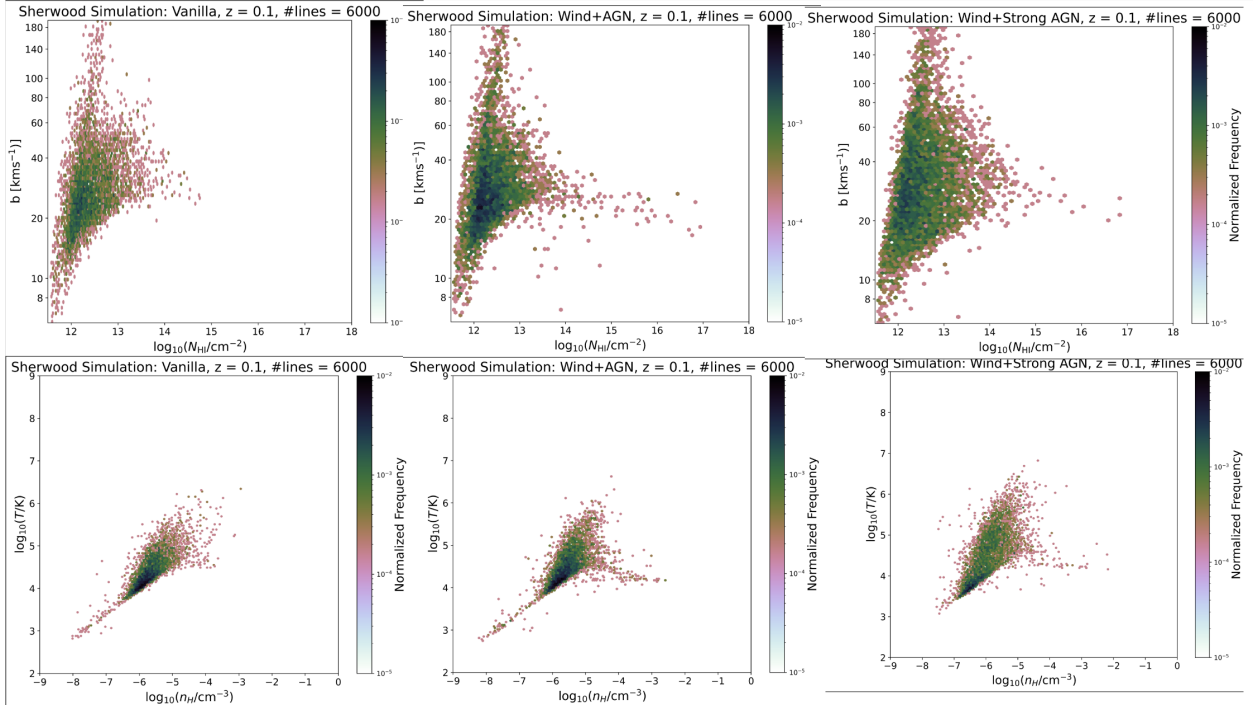


Figure 3.8 Distribution of 6000 absorbers in N_{HI} - b plane (top) and T - ρ plane (bottom) at $z=0.1$ for no feedback (Left), wind+AGN (middle) and wind+strongAGN (Right) simulation runs.

After this we investigate the distribution of the absorbers in the N_{HI} - b plane, as well as the T - ρ plane. Figure 3.8 shows the preliminary results of such an analysis at $z=0.1$. We see that the distribution of the absorbers for different feedback physics is significantly different. Without any feedback there is no high density gas cloud as the cold dense gas has already been accreted by the galaxies to form stars and the hot gas is not detectable via the Ly α forest. The gas in wind+AGN run seems promising as the turnover is clear in the T - ρ plane and we can also see a hint of a turn over in the N_{HI} - b plane. Further analysis such as fitting a power-law and how the turnover evolves with redshift is required for a better understanding. The gas in the wind+strongAGN run on the other hand is widely distributed along the vertical (temperature) axis and very few absorbers are in the high density+cold temperature region. However we do see a turnover and it should be more visible as we fit more spectra. We also need to investigate how different the T - ρ relation is compared to the wind+AGN run. In contrast, at $z=2.4$, Figure 3.9 shows little difference between the no feedback and wind+strongAGN run. This is consistent with what we saw in our individual halo analyses.

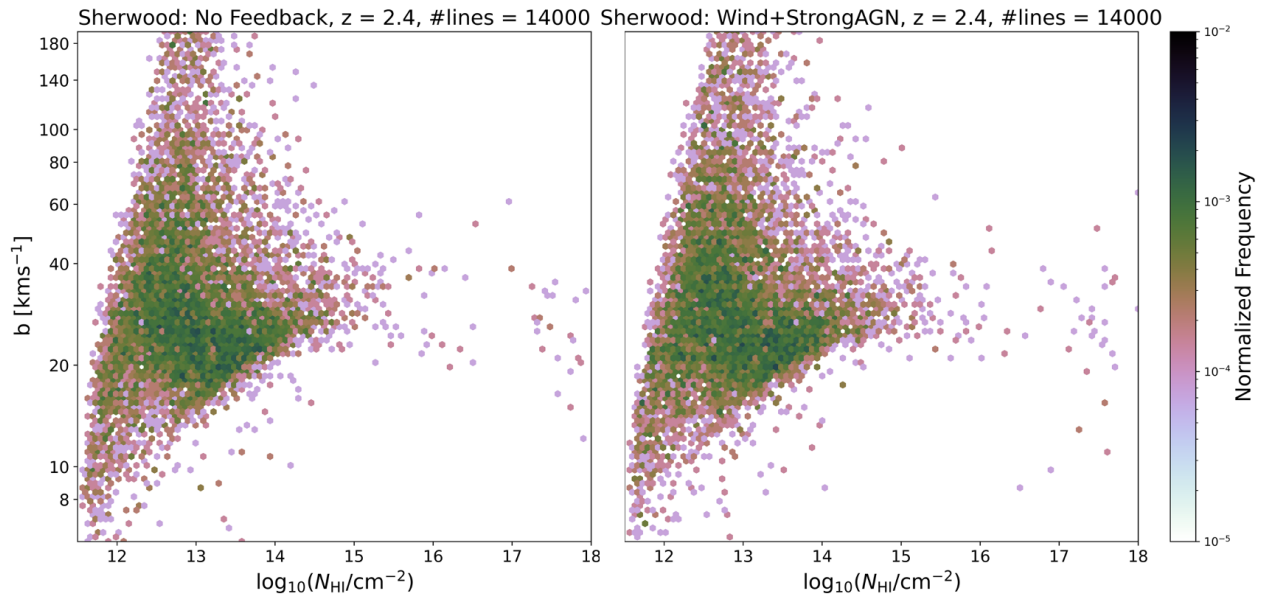


Figure 3.9 Line width (b) vs column density distribution of 14000 Ly α absorbers from random LOSs at $z=2.4$ in the Sherwood No feedback (*left*) and wind+strongAGN (*right*) runs. The wind+strongAGN absorbers seem to have a significantly wider distribution along the b -axis which is expected from a hotter IGM. However, in the CGM region, number of absorbers is still very sparse. A similar analysis needed by targeting LOSs nearby galaxies to investigate this region further.

CHAPTER 4

TIMELINE AND FUTURE WORK

In conclusion, we return to the questions posed in Chapter 1 focusing on those that my PhD will address. We summarize progress so far, and outline future work. We summarize an additional project not included in the proposal, note publications and presentations to date, and present a timeline of anticipated milestones.

4.1 Work to date and future work

- **How accurately do cosmological simulations represent the CGM around galaxies of different masses and in the redshift range $0 < z < 4$?**

So far, I have obtained spectra on random LOSs for two redshift bins for each of the Sherwood (for each physics) and IllustrisTNG simulations. At low redshift, out of 16,000 LOSs/ box, all have been fitted using VPFIT to obtain the column density and linewidth of the absorbers. I will obtain spectra on random LOSs for at least three additional redshift bins per Sherwood physics, and for IllustrisTNG-100, and carry out profile fitting analysis.

My Co-advisor Dr. Kim is analyzing new spectroscopic data, making a larger observational sample with more absorbers at CGM column densities. We will then statistically compare the properties of absorbers seen in simulations with those seen in the universe.

- **What is the impact of feedback processes on the properties of the CGM, and how do these effects vary across different galaxy populations?**

I have obtained examples of targeted spectra on LOSs at specific impact parameters around halos, and fit absorption profiles.

As a function of impact parameter and halo mass bin, I will obtain and fit samples of targeted spectra - of order 1000 per box, to be determined. This will be carried out for the two current redshifts under consideration and at least three additional ones as outlined in the point above.

This will allow a detailed comparison of line profiles as a function of galaxy mass, impact parameter and implemented subgrid physics.

- **Is it possible to quantify the effect of feedback processes on the turbulence and ionization state of the CGM gas?**

To look at the effect of turbulence, we need to compute the non-thermal velocities in the gas clouds. To imitate observations, where turbulence is computed using eq. 2.20 by comparing the line-width of two different species in the same gas cloud, I will calculate metal abundance in the Sherwood simulations. I will then extract metal absorption lines similar to HI absorption lines and calculate $b_{\text{non-thermal}}$ from comparing

HI and absorption lines. This analysis will then be compared to similar analysis in observations.

- **How big is the extent of the CGM around galaxies and how does it evolve with redshift?**

Once we detect a CGM $T_{\min}\text{-}\rho$ cutoff relation, we will try different fitting algorithms similar to Rudie et al. (2012) to fit the cutoff relation. We plan to come up of our own algorithm if none of the already existing ones work. Using both $T_{\min}\text{-}\rho$ relation in the IGM and the CGM we will define a turnover point in the the $T\text{-}\rho$ plane which will effectively define the extent of CGM. We will also investigate how the CGM size evolves with time by doing the same analysis at different redshifts.

4.2 Application of Machine Learning

In collaboration with Sujin Hwang (CS) we are training Machine Learning (ML) models using the synthetic spectra obtained from cosmological simulations. The goal of this project is to identify the cosmological simulations (with implemented physics) that best agree with observed spectra, and to better understand degeneracies between different subgrid physics. This project is in the early stages, exploring data compression and preparation methods and identifying the best architectures for our purposes.

4.3 Additional Project: Cluster Mergers

I have worked with Dr. Sharon Felix and undergraduates Kate Shavelle (U. Columbia, now Princeton) and Brandon Sike (UTD, now U. Michigan) on a project related to cluster merger simulations (Felix et al., 2024). We modeled JKCS041, one of the most distant galaxy clusters in the Universe for which resolved X-ray and SZ measurements are available. This necessitated a cluster merger scenario in an ideal (isolated) simulation using GAMER-2 (Schive et al., 2018). We plan to extend such work on cluster mergers to cosmological simulations, where clusters have realistic shapes, substructure and surrounding large scale structure. We have recently acquired access to the TNG-Cluster simulation which is a large scale 1 Gpc³ extension of the IllustrisTNG suite (Nelson et al., 2024). With Kate Brown and Nicolas Mazziotti (NSF REU students in summer 2024 at UTD and Maria Mitchell Observatory, respectively), we have been using the TNG-Cluster data to mine cluster mergers and look for systems identical to Abell 2146, which is an interesting system since idealized simulations have not reproduced some of the observational features (such as discrepant X-ray and lensing masses) (Chadayammuri et al., 2021), and analogues of JKCS041. Also involved in this project is UTD undergraduate Lauren Mangu, and Brandon Sike.

4.4 Products during PhD

Publication: Decoding the early Universe: exploring a merger scenario for the high-redshift cluster JKCS041 using numerical models

Sharon Felix, Antareep Gogoi, Kaitlyn Shavelle, Brandon Sike, Lindsay King, Stefano Andreon, Urmila Chadayammuri, John ZuHone, Charles Romero

Monthly Notices of the Royal Astronomical Society, Volume 534, Issue 4, November 2024, Pages 3676–3687, <https://doi.org/10.1093/mnras/stae2338>

Contribution and skills - Gained skills in performing idealized numerical simulations and using Texas Advanced Computing Center. Developed mentoring skills (Kate Shavelle and Brandon Sike). Contributed to running and analyzing idealized simulations.

External Presentations:

- Spring 2022, TACOS at SMU. fireslide presentation.
- Spring 2024, Presentation at Astronomical Observatory of Trieste, Italy (hosted by SISSA)
- Spring 2024, Presentation at Nottingham University, UK
- Presentation at UNT-UTD PAARE astronomy symposium, UNT, Denton
- Fall 2024, TX-Section APS presentation at SMU

Public Engagement:

- Collaborated with ArtSci Lab in UTD ATEC department in the Project "Sensing Deep Space: Pandora's Cluster".
- Collaborated with CADRE Media Lab at San Jose State University to in a data sonification project.

4.5 Timeline of anticipated milestones

4/2025 - Complete paper on temperature-density relation from simulations

Spring 2025 - If current training of ML models is successful, brief paper will be written in spring 2025

11/2025 Complete paper on investigating Abell 2146 and JKCS041 using large volume cosmological simulations

5/2026 Thesis defense

REFERENCES

- Bahcall, J. N. and E. E. Salpeter (1965, November). On the Interaction of Radiation from Distant Sources with the Intervening Medium. *142*, 1677–1680.
- Baldwin, J. A. (1977, June). Luminosity Indicators in the Spectra of Quasi-Stellar Objects. *214*, 679–684.
- Barnes, J. and P. Hut (1986, December). A hierarchical $O(N \log N)$ force-calculation algorithm. *324*(6096), 446–449.
- Behroozi, P. S., R. H. Wechsler, and H.-Y. Wu (2013, January). The ROCKSTAR Phase-space Temporal Halo Finder and the Velocity Offsets of Cluster Cores. *762*(2), 109.
- Bolton, J. S., P. Gaikwad, M. G. Haehnelt, T.-S. Kim, F. Nasir, E. Puchwein, M. Viel, and B. P. Wakker (2022, March). Limits on non-canonical heating and turbulence in the intergalactic medium from the low redshift lyman forest. *Monthly Notices of the Royal Astronomical Society* *513*(1), 864–885.
- Bolton, J. S., E. Puchwein, D. Sijacki, M. G. Haehnelt, T.-S. Kim, A. Meiksin, J. A. Regan, and M. Viel (2017, January). The Sherwood simulation suite: overview and data comparisons with the Lyman α forest at redshifts $2 \leq z \leq 5$. *464*(1), 897–914.
- Carswell, R. F. and J. K. Webb (2014, August). VPFIT: Voigt profile fitting program. Astrophysics Source Code Library, record ascl:1408.015.
- Cen, R., J. Miralda-Escudé, J. P. Ostriker, and M. Rauch (1994, December). Gravitational Collapse of Small-Scale Structure as the Origin of the Lyman-Alpha Forest. *437*, L9.
- Cen, R. and J. P. Ostriker (1999, March). Where Are the Baryons? *514*(1), 1–6.
- Chadayammuri, U., J. ZuHone, P. Nulsen, D. Nagai, S. Felix, F. Andrade-Santos, L. King, and H. Russell (2021, October). Constraining merging galaxy clusters with x-ray and lensing simulations and observations: the case of abell 2146. *Monthly Notices of the Royal Astronomical Society* *509*(1), 1201–1216.
- Chatzikos, M., S. Bianchi, F. Camilloni, P. Chakraborty, C. M. Gunasekera, F. Guzmán, J. S. Milby, A. Sarkar, G. Shaw, P. A. M. van Hoof, and G. J. Ferland (2023). The 2023 release of cloudy.
- Chen, H., K. M. Lanzetta, J. K. Webb, and X. Barcons (2001, October). The gaseous extent of galaxies and the origin of ly absorption systems. v. optical and near-infrared photometry of ly-absorbing galaxies atzlt;1. *The Astrophysical Journal* *559*(2), 654–674.

- Croton, D. J., V. Springel, S. D. M. White, G. De Lucia, C. S. Frenk, L. Gao, A. Jenkins, G. Kauffmann, J. F. Navarro, and N. Yoshida (2006, January). The many lives of active galactic nuclei: cooling flows, black holes and the luminosities and colours of galaxies. *365*(1), 11–28.
- Davé, R., B. D. Oppenheimer, N. Katz, J. A. Kollmeier, and D. H. Weinberg (2010, November). The intergalactic medium over the last 10 billion years - I. Ly α absorption and physical conditions. *408*(4), 2051–2070.
- Demtröder, W. (2008). *Laser Spectroscopy: Vol. 1: Basic Principles*. Laser Spectroscopy. Springer Berlin Heidelberg.
- Efstathiou, G., M. Davis, S. D. M. White, and C. S. Frenk (1985, February). Numerical techniques for large cosmological N-body simulations. *57*, 241–260.
- Faucher-Giguere, C.-A. and S. P. Oh (2023). Key physical processes in the circumgalactic medium.
- Felix, S., A. Gogoi, K. Shavelle, B. Sike, L. King, S. Andreon, U. Chadayammuri, J. ZuHone, and C. Romero (2024, November). Decoding the early Universe: exploring a merger scenario for the high-redshift cluster JKCS041 using numerical models. *534*(4), 3676–3687.
- Gallo, E., R. P. Fender, and G. G. Pooley (2003, September). A universal radio-X-ray correlation in low/hard state black hole binaries. *344*(1), 60–72.
- Gingold, R. A. and J. J. Monaghan (1977, November). Smoothed particle hydrodynamics: theory and application to non-spherical stars. *181*, 375–389.
- Gunn, J. E. and B. A. Peterson (1965, November). On the Density of Neutral Hydrogen in Intergalactic Space. *142*, 1633–1636.
- Haardt, F. and P. Madau (2012, February). Radiative Transfer in a Clumpy Universe. IV. New Synthesis Models of the Cosmic UV/X-Ray Background. *746*(2), 125.
- Hernquist, L., N. Katz, D. H. Weinberg, and J. Miralda-Escude (1996). The Lyman alpha forest in the cold dark matter model. *Astrophys. J. Lett.* *457*, L51.
- Hiss, H., M. Walther, J. F. Hennawi, J. Oñorbe, J. M. O'Meara, A. Rorai, and Z. Lukić (2018, September). A new measurement of the temperature-density relation of the igm from voigt profile fitting. *The Astrophysical Journal* *865*(1), 42.
- Hjerting, F. (1938, November). Tables Facilitating the Calculation of Line Absorption Coefficients. *88*, 508.

- Hu, E. M., T.-S. Kim, L. L. Cowie, A. Songaila, and M. Rauch (1995, October). The distribution of column densities and b values in the lyman-alpha forest. *The Astronomical Journal* *110*, 1526.
- Hu, W. and S. Dodelson (2002). Cosmic Microwave Background Anisotropies. *Ann. Rev. Astron. Astrophys.* *40*, 171–216.
- Hui, L. and N. Y. Gnedin (1997, November). Equation of state of the photoionized intergalactic medium. *292*(1), 27–42.
- Kennicutt, Robert C., J. (1998, May). The Global Schmidt Law in Star-forming Galaxies. *498*(2), 541–552.
- Kim, T. S., J. S. Bolton, M. Viel, M. G. Haehnelt, and R. F. Carswell (2007, December). An improved measurement of the flux distribution of the Ly α forest in QSO absorption spectra: the effect of continuum fitting, metal contamination and noise properties. *382*(4), 1657–1674.
- Kim, T.-S., E. M. Hu, L. L. Cowie, and A. Songaila (1997, July). The Redshift Evolution of the Ly alpha Forest. *114*, 1–13.
- Lanzetta, K. M., D. V. Bowen, D. Tytler, and J. K. Webb (1995, April). The Gaseous Extent of Galaxies and the Origin of Lyman-Alpha Absorption Systems: A Survey of Galaxies in the Fields of Hubble Space Telescope Spectroscopic Target QSOs. *442*, 538.
- Lewis, A., A. Challinor, and A. Lasenby (2000, August). Efficient Computation of Cosmic Microwave Background Anisotropies in Closed Friedmann-Robertson-Walker Models. *538*(2), 473–476.
- Lucy, L. B. (1977, December). A numerical approach to the testing of the fission hypothesis. *82*, 1013–1024.
- Lynds, R. (1971, March). The Absorption-Line Spectrum of 4c 05.34. *164*, L73.
- Martizzi, D., M. Vogelsberger, M. C. Artale, M. Haider, P. Torrey, F. Marinacci, D. Nelson, A. Pillepich, R. Weinberger, L. Hernquist, J. Naiman, and V. Springel (2019, July). Baryons in the Cosmic Web of IllustrisTNG - I: gas in knots, filaments, sheets, and voids. *486*(3), 3766–3787.
- Münch, G. and H. Zirin (1961, January). Interstellar Matter at Large Distances from the Galactic Plane. *133*, 11.
- Murphy, M. T., G. G. Kacprzak, G. A. D. Savorgnan, and R. F. Carswell (2019). The uves spectral quasar absorption database (squad) data release 1: the first 10 million seconds. *MNRAS* *482*, 3458.

- Nelson, D., A. Pillepich, M. Ayromlou, W. Lee, K. Lehle, E. Rohr, and N. Truong (2024). Introducing the tng-cluster simulation: overview and physical properties of the gaseous intracluster medium.
- O'Meara, J. M., N. Lehner, J. C. Howk, J. X. Prochaska, A. J. Fox, M. A. Swain, C. R. Gelino, G. B. Berriman, and H. Tran (2015, October). The First Data Release of the KODIAQ Survey. *150*(4), 111.
- Peebles, P. J. E. (1980). *The large-scale structure of the universe*.
- Peeples, M., J. Tumlinson, A. Fox, A. Aloisi, S. Fleming, R. Jedrzejewski, C. Oliveira, T. Ayres, C. Danforth, B. Keeney, and E. Jenkins (2017, April). The Hubble Spectroscopic Legacy Archive. Instrument Science Report COS 2017-4, 8 pages.
- Peeples, M. S., D. H. Weinberg, R. Davé, M. A. Fardal, and N. Katz (2010, May). Pressure support versus thermal broadening in the Lyman α forest - I. Effects of the equation of state on longitudinal structure. *404*(3), 1281–1294.
- Penzias, A. A. and R. W. Wilson (1965, July). A Measurement of Excess Antenna Temperature at 4080 Mc/s. *142*, 419–421.
- Pillepich, A., V. Springel, D. Nelson, S. Genel, J. Naiman, R. Pakmor, L. Hernquist, P. Torrey, M. Vogelsberger, R. Weinberger, and F. Marinacci (2017, October). Simulating galaxy formation with the *illustris*tng model. *Monthly Notices of the Royal Astronomical Society* *473*(3), 4077–4106.
- Planck Collaboration, P. A. R. Ade, N. Aghanim, C. Armitage-Caplan, M. Arnaud, M. Ashdown, F. Atrio-Barandela, J. Aumont, C. Baccigalupi, A. J. Banday, R. B. Barreiro, J. G. Bartlett, E. Battaner, K. Benabed, A. Benoît, A. Benoit-Lévy, J. P. Bernard, M. Bersanelli, P. Bielewicz, J. Bobin, J. J. Bock, A. Bonaldi, J. R. Bond, J. Borrill, F. R. Bouchet, M. Bridges, M. Bucher, C. Burigana, R. C. Butler, E. Calabrese, B. Capellini, J. F. Cardoso, A. Catalano, A. Challinor, A. Chamballu, R. R. Chary, X. Chen, H. C. Chiang, L. Y. Chiang, P. R. Christensen, S. Church, D. L. Clements, S. Colombi, L. P. L. Colombo, F. Couchot, A. Coulais, B. P. Crill, A. Curto, F. Cuttaia, L. Danese, R. D. Davies, R. J. Davis, P. de Bernardis, A. de Rosa, G. de Zotti, J. Delabrouille, J. M. Delouis, F. X. Désert, C. Dickinson, J. M. Diego, K. Dolag, H. Dole, S. Donzelli, O. Doré, M. Douspis, J. Dunkley, X. Dupac, G. Efstathiou, F. Elsner, T. A. Enßlin, H. K. Eriksen, F. Finelli, O. Forni, M. Frailis, A. A. Fraisse, E. Franceschi, T. C. Gaier, S. Galeotta, S. Galli, K. Ganga, M. Giard, G. Giardino, Y. Giraud-Héraud, E. Gjerløw, J. González-Nuevo, K. M. Górska, S. Gratton, A. Gregorio, A. Gruppuso, J. E. Gudmundsson, J. Haissinski, J. Hamann, F. K. Hansen, D. Hanson, D. Harrison, S. Henrot-Versillé, C. Hernández-Monteagudo, D. Herranz, S. R. Hildebrandt, E. Hivon, M. Hobson, W. A. Holmes, A. Hornstrup, Z. Hou, W. Hovest, K. M. Huffenberger, A. H. Jaffe, T. R. Jaffe, J. Jewell, W. C. Jones, M. Juvela, E. Keihänen, R. Keskitalo, T. S. Kisner,

R. Kneissl, J. Knoche, L. Knox, M. Kunz, H. Kurki-Suonio, G. Lagache, A. Lähteenmäki, J. M. Lamarre, A. Lasenby, M. Lattanzi, R. J. Laureijs, C. R. Lawrence, S. Leach, J. P. Leahy, R. Leonardi, J. León-Tavares, J. Lesgourgues, A. Lewis, M. Liguori, P. B. Lilje, M. Linden-Vørnle, M. López-Caniego, P. M. Lubin, J. F. Macías-Pérez, B. Maffei, D. Maino, N. Mandolesi, M. Maris, D. J. Marshall, P. G. Martin, E. Martínez-González, S. Masi, M. Massardi, S. Matarrese, F. Matthai, P. Mazzotta, P. R. Meinhold, A. Melchiorri, J. B. Melin, L. Mendes, E. Menegoni, A. Mennella, M. Migliaccio, M. Millea, S. Mitra, M. A. Miville-Deschénes, A. Moneti, L. Montier, G. Morgante, D. Mortlock, A. Moss, D. Munshi, J. A. Murphy, P. Naselsky, F. Nati, P. Natoli, C. B. Netterfield, H. U. Nørgaard-Nielsen, F. Noviello, D. Novikov, I. Novikov, I. J. O'Dwyer, S. Osborne, C. A. Oxborrow, F. Paci, L. Pagano, F. Pajot, R. Paladini, D. Paoletti, B. Partridge, F. Pasian, G. Patanchon, D. Pearson, T. J. Pearson, H. V. Peiris, O. Perdereau, L. Perotto, F. Perrotta, V. Pettorino, F. Piacentini, M. Piat, E. Pierpaoli, D. Pietrobon, S. Plaszczynski, P. Platania, E. Pointecouteau, G. Polenta, N. Ponthieu, L. Popa, T. Poutanen, G. W. Pratt, G. Prézeau, S. Prunet, J. L. Puget, J. P. Rachen, W. T. Reach, R. Rebolo, M. Reinecke, M. Remazeilles, C. Renault, S. Ricciardi, T. Riller, I. Ristorcelli, G. Rocha, C. Rosset, G. Roudier, M. Rowan-Robinson, J. A. Rubiño-Martín, B. Rusholme, M. Sandri, D. Santos, M. Savelainen, G. Savini, D. Scott, M. D. Seiffert, E. P. S. Shellard, L. D. Spencer, J. L. Starck, V. Stolyarov, R. Stompor, R. Sudiwala, R. Sunyaev, F. Sureau, D. Sutton, A. S. Suur-Uski, J. F. Sygnet, J. A. Tauber, D. Tavagnacco, L. Terenzi, L. Toffolatti, M. Tomasi, M. Tristram, M. Tucci, J. Tuovinen, M. Türler, G. Umana, L. Valenziano, J. Valiviita, B. Van Tent, P. Vielva, F. Villa, N. Vittorio, L. A. Wade, B. D. Wandelt, I. K. Wehus, M. White, S. D. M. White, A. Wilkinson, D. Yvon, A. Zacchei, and A. Zonca (2014, November). Planck 2013 results. XVI. Cosmological parameters. 571, A16.

Planck Collaboration, P. A. R. Ade, N. Aghanim, M. Arnaud, M. Ashdown, J. Aumont, C. Baccigalupi, A. J. Banday, R. B. Barreiro, J. G. Bartlett, N. Bartolo, E. Battaner, R. Battye, K. Benabed, A. Benoît, A. Benoit-Lévy, J. P. Bernard, M. Bersanelli, P. Bielewicz, J. J. Bock, A. Bonaldi, L. Bonavera, J. R. Bond, J. Borrill, F. R. Bouchet, F. Boulanger, M. Bucher, C. Burigana, R. C. Butler, E. Calabrese, J. F. Cardoso, A. Catalano, A. Challinor, A. Chamballu, R. R. Chary, H. C. Chiang, J. Chluba, P. R. Christensen, S. Church, D. L. Clements, S. Colombi, L. P. L. Colombo, C. Combet, A. Coulais, B. P. Crill, A. Curto, F. Cuttaia, L. Danese, R. D. Davies, R. J. Davis, P. de Bernardis, A. de Rosa, G. de Zotti, J. Delabrouille, F. X. Désert, E. Di Valentino, C. Dickinson, J. M. Diego, K. Dolag, H. Dole, S. Donzelli, O. Doré, M. Douspis, A. Ducout, J. Dunkley, X. Dupac, G. Efstathiou, F. Elsner, T. A. Enßlin, H. K. Eriksen, M. Farhang, J. Fergusson, F. Finelli, O. Forni, M. Frailis, A. A. Fraisse, E. Franceschi, A. Frejsel, S. Galeotta, S. Galli, K. Ganga, C. Gauthier, M. Gerbino, T. Ghosh, M. Giard, Y. Giraud-Héraud, E. Giusarma, E. Gjerløw, J. González-Nuevo, K. M. Górska, S. Gratton, A. Gregorio, A. Gruppuso, J. E. Gudmundsson, J. Hamann, F. K. Hansen, D. Hanson, D. L. Harrison, G. Helou, S. Henrot-Versillé, C. Hernández-Monteagudo, D. Herranz, S. R. Hildebrandt, E. Hivon, M. Hobson, W. A. Holmes, A. Hornstrup, W. Hovest, Z. Huang, K. M. Huffenberger, G. Hurier, A. H.

Jaffe, T. R. Jaffe, W. C. Jones, M. Juvela, E. Keihänen, R. Keskitalo, T. S. Kisner, R. Kneissl, J. Knoche, L. Knox, M. Kunz, H. Kurki-Suonio, G. Lagache, A. Lähteenmäki, J. M. Lamarre, A. Lasenby, M. Lattanzi, C. R. Lawrence, J. P. Leahy, R. Leonardi, J. Lesgourgues, F. Levrier, A. Lewis, M. Liguori, P. B. Lilje, M. Linden-Vørnle, M. López-Caniego, P. M. Lubin, J. F. Macías-Pérez, G. Maggio, D. Maino, N. Mandolesi, A. Mangilli, A. Marchini, M. Maris, P. G. Martin, M. Martinelli, E. Martínez-González, S. Masi, S. Matarrese, P. McGehee, P. R. Meinholt, A. Melchiorri, J. B. Melin, L. Mendes, A. Menella, M. Migliaccio, M. Millea, S. Mitra, M. A. Miville-Deschénes, A. Moneti, L. Montier, G. Morgante, D. Mortlock, A. Moss, D. Munshi, J. A. Murphy, P. Naselsky, F. Nati, P. Natoli, C. B. Netterfield, H. U. Nørgaard-Nielsen, F. Noviello, D. Novikov, I. Novikov, C. A. Oxborrow, F. Paci, L. Pagano, F. Pajot, R. Paladini, D. Paoletti, B. Partridge, F. Pasian, G. Patanchon, T. J. Pearson, O. Perdereau, L. Perotto, F. Perrotta, V. Pettorino, F. Piacentini, M. Piat, E. Pierpaoli, D. Pietrobon, S. Plaszczynski, E. Pointecouteau, G. Polenta, L. Popa, G. W. Pratt, G. Prézeau, S. Prunet, J. L. Puget, J. P. Rachén, W. T. Reach, R. Rebolo, M. Reinecke, M. Remazeilles, C. Renault, A. Renzi, I. Ristorcelli, G. Rocha, C. Rosset, M. Rossetti, G. Roudier, B. Rouillé d'Orfeuil, M. Rowan-Robinson, J. A. Rubiño-Martín, B. Rusholme, N. Said, V. Salvatelli, L. Salvati, M. Sandri, D. Santos, M. Savelainen, G. Savini, D. Scott, M. D. Seiffert, P. Serra, E. P. S. Shellard, L. D. Spencer, M. Spinelli, V. Stolyarov, R. Stompor, R. Sudiwala, R. Sunyaev, D. Sutton, A. S. Suur-Uski, J. F. Sygnet, J. A. Tauber, L. Terenzi, L. Toffolatti, M. Tomasi, M. Tristram, T. Trombetti, M. Tucci, J. Tuovinen, M. Türler, G. Umana, L. Valenziano, J. Valiviita, F. Van Tent, P. Vielva, F. Villa, L. A. Wade, B. D. Wandelt, I. K. Wehus, M. White, S. D. M. White, A. Wilkinson, D. Yvon, A. Zacchei, and A. Zonca (2016, September). Planck 2015 results. XIII. Cosmological parameters. *594*, A13.

Press, W. H. and P. Schechter (1974, February). Formation of Galaxies and Clusters of Galaxies by Self-Similar Gravitational Condensation. *187*, 425–438.

Puchwein, E., J. S. Bolton, L. C. Keating, M. Molaro, P. Gaikwad, G. Kulkarni, M. G. Haehnelt, V. Iršič, T. Šoltinský, M. Viel, D. Aubert, G. D. Becker, and A. Meiksin (2022, December). The sherwood-relics simulations: overview and impact of patchy reionization and pressure smoothing on the intergalactic medium. *Monthly Notices of the Royal Astronomical Society* *519*(4), 6162–6183.

Puchwein, E. and V. Springel (2013, February). Shaping the galaxy stellar mass function with supernova- and AGN-driven winds. *428*(4), 2966–2979.

Rees, M. J. (1998). (*NAS Colloquium*) *The Age of the Universe, Dark Matter, and Structure Formation*. Washington, DC: The National Academies Press.

Rudie, G. C., C. C. Steidel, and M. Pettini (2012, October). The Temperature-Density Relation in the Intergalactic Medium at Redshift $z = 2.4$. *757*(2), L30.

- Rudie, G. C., C. C. Steidel, and M. Pettini (2012, September). The temperature-density relation in the intergalactic medium at redshift $\langle z \rangle = 2.4$. *The Astrophysical Journal* 757(2), L30.
- Sargent, W. L. W., P. J. Young, A. Boksenberg, and D. Tytler (1980, January). The distribution of Lyman-alpha absorption lines in the spectra of six QSOs: evidence for an intergalactic origin. 42, 41–81.
- Schaye, J., T. Theuns, M. Rauch, G. Efstathiou, and W. L. W. Sargent (2000, November). The thermal history of the intergalactic medium*. 318(3), 817–826.
- Schive, H.-Y., J. A. ZuHone, N. J. Goldbaum, M. J. Turk, M. Gaspari, and C.-Y. Cheng (2018, December). GAMER-2: a GPU-accelerated adaptive mesh refinement code - accuracy, performance, and scalability. 481(4), 4815–4840.
- Schmidt, M. (1965, April). Large Redshifts of Five Quasi-Stellar Sources. 141, 1295.
- Sijacki, D., V. Springel, T. Di Matteo, and L. Hernquist (2007, August). A unified model for agn feedback in cosmological simulations of structure formation: Agn feedback in cosmological simulations. *Monthly Notices of the Royal Astronomical Society* 380(3), 877–900.
- Spitzer, Lyman, J. (1956, July). On a Possible Interstellar Galactic Corona. 124, 20.
- Springel, V. (2005, December). The cosmological simulation code gadget-2. *Monthly Notices of the Royal Astronomical Society* 364(4), 1105–1134.
- Springel, V. and L. Hernquist (2003, February). Cosmological smoothed particle hydrodynamics simulations: a hybrid multiphase model for star formation. 339(2), 289–311.
- Springel, V., R. Pakmor, A. Pillepich, R. Weinberger, D. Nelson, L. Hernquist, M. Vogelsberger, S. Genel, P. Torrey, F. Marinacci, and J. Naiman (2018, March). First results from the IllustrisTNG simulations: matter and galaxy clustering. 475(1), 676–698.
- Springel, V., S. D. M. White, G. Tormen, and G. Kauffmann (2001, December). Populating a cluster of galaxies - I. Results at $z=0$. 328(3), 726–750.
- Steidel, C. C., D. K. Erb, A. E. Shapley, M. Pettini, N. Reddy, M. Bogosavljević, G. C. Rudie, and O. Rakic (2010, July). The Structure and Kinematics of the Circumgalactic Medium from Far-ultraviolet Spectra of $z \sim 2$ -3 Galaxies. 717(1), 289–322.
- Theuns, T., A. Leonard, G. Efstathiou, F. R. Pearce, and P. A. Thomas (1998, December). P $\hat{3}$ M-SPH simulations of the Lyalpha forest. 301(2), 478–502.

- Tumlinson, J., M. S. Peebles, and J. K. Werk (2017, August). The circumgalactic medium. *Annual Review of Astronomy and Astrophysics* 55(1), 389–432.
- Vogelsberger, M., S. Genel, D. Sijacki, P. Torrey, V. Springel, and L. Hernquist (2013, December). A model for cosmological simulations of galaxy formation physics. 436(4), 3031–3067.
- Vogelsberger, M., S. Genel, V. Springel, P. Torrey, D. Sijacki, D. Xu, G. Snyder, D. Nelson, and L. Hernquist (2014, October). Introducing the Illustris Project: simulating the coevolution of dark and visible matter in the Universe. 444(2), 1518–1547.
- Vogt, S. S., S. L. Allen, B. C. Bigelow, L. Bresee, B. Brown, T. Cantrall, A. Conrad, M. Couture, C. Delaney, H. W. Epps, D. Hilyard, D. F. Hilyard, E. Horn, N. Jern, D. Kanto, M. J. Keane, R. I. Kibrick, J. W. Lewis, J. Osborne, G. H. Pardeilhan, T. Pfister, T. Ricketts, L. B. Robinson, R. J. Stover, D. Tucker, J. Ward, and M. Z. Wei (1994, June). HIRES: the high-resolution echelle spectrometer on the Keck 10-m Telescope. In D. L. Crawford and E. R. Craine (Eds.), *Instrumentation in Astronomy VIII*, Volume 2198 of *Society of Photo-Optical Instrumentation Engineers (SPIE) Conference Series*, pp. 362.
- Weinberger, R., V. Springel, L. Hernquist, A. Pillepich, F. Marinacci, R. Pakmor, D. Nelson, S. Genel, M. Vogelsberger, J. Naiman, and P. Torrey (2017, March). Simulating galaxy formation with black hole driven thermal and kinetic feedback. 465(3), 3291–3308.
- Weinberger, R., V. Springel, and R. Pakmor (2020, June). The arepo public code release. *The Astrophysical Journal Supplement Series* 248(2), 32.